Microdissected tumor cuboids: a microscale cancer model for large-scale testing that retains a complex tumor microenvironment

Lisa F Horowitz[1#], Ricard Rodriguez-Mias[2], Marina Chan[3], SongLi Zhu[3], Noah R Gottshall[1], Ivan Stepanov[1,4], Casey Stiles[1,5], Marcus Yeung[3], Tran NH Nguyen[1,6], Ethan J Lockhart[1], Raymond S Yeung[7], Judit Villen[2], Taranjit S Gujral[3], and Albert Folch[1]

[1] Department of Bioengineering, University of Washington, Seattle, WA, USA.
[2] Department of Genome Sciences, University of Washington, Seattle, WA, USA.
[3] Human Biology Division, Fred Hutchinson Cancer Center, Seattle, WA, USA.
[4] Department of Mechanical Engineering, University of Washington, Seattle, WA, USA.
[5] Department of Chemical Engineering, University of Washington, Seattle, WA, USA.
[6] Department of Biochemistry, University of Washington, Seattle, WA, USA.
[7] Department of Surgery, University of Washington, Seattle, WA, USA.
[#] Email: lisafh@uw.edu

ABSTRACT

Current cancer disease models fail to faithfully recapitulate key features of the human tumor microenvironment (TME), such as immune and vascular cells, while simultaneously enabling high-throughput drug tests. We have recently developed a precision slicing method that optimizes the yield of large numbers of cuboidal microtissues ("cuboids", ~(400 µm)^3) from a single tumor biopsy. Here we demonstrate that cuboids from syngeneic mouse tumor models and human tumors retain a complex TME, making them amenable for drug and immunotherapy evaluation. We characterize relevant TME parameters, such as cellular architecture, cytokine secretion, proteomics profiles, and response to drug panels in multi-well arrays. Despite the cutting procedure and the time spent in culture (up to 7 days), the cuboids display strong cytokine and drug responses, including to immunotherapy. Overall, our results suggest that cuboids could provide invaluable therapeutic information for personalized oncology applications, and could help the development of TME-dependent therapeutics and cancer disease models, including for clinical trials.

INTRODUCTION

To bridge the gap between bench and bedside, more faithful models of human cancers that can inform large-scale drug tests are needed.[1] For almost a century, researchers have relied on models such as tissue cultures and patient-derived xenografts (PDXs). PDXs permit the study of drug responses and tumor evolution (*e.g.*, tumorigenesis and metastasis) in an intact organism, however they have critical limitations. First, in PDXs most of the tumor microenvironment (TME) is from the host mouse and PDXs from individual patients grow too slow to inform initial post-operative therapeutic decisions. Second, PDXs grow faster compared to human tumors, hence respond better to antiproliferative drugs – so testing these drugs in PDXs can yield an inaccurate measure of their efficacy in humans.[2] Third, the PDX TME lacks tumor heterogeneity (particularly the stromal component[3]), molecular transformation events, and drug resistance mechanisms seen in the human TME.[2,4] Finally, since the mice are immune deficient, testing of immunomodulatory agents is not possible.[1,4] ('Humanized' mice[5] are immune competent but still have rodent-derived stroma.)

Microscale cancer models such as organoids or microdissected tissues have many valuable features that make them highly complementary to macroscale full-animal models: i) they enable multiplexing of drug tests by miniaturized fluid handling such as microfluidics;[6] ii) they enable inexpensive, more efficient tests with high clinical biomimicry using human cells;[7] iii) they retain the structural features of the heterogeneous TME to properly address, target, and understand the contributions of these unique zones

to therapeutic response;[8,9] iv) they help maintain *ex vivo* viability by facilitating diffusive mass transport to the inside of the tissue after surgical extraction of the tissue and interruption of vascular (convective) mass transport;[10,11] v) they maximize the use of scarce biopsies;[12,13] and vi) they minimize animal testing (an advantage at a time when growing sectors of society are questioning animal experimentation[14]).

In the last decade, microscale cancer models such as patient-derived organoids[15] (PDOs) (also termed "tumor spheroids") and organs-on-chips[16] (OOCs) have revealed the power and clinical relevance of *ex vivo* testing of cancer patient tissue. However, in these platforms, which often take weeks to months to establish, the tumor tissue is generated *de novo* by growing the patient's cancer cells.[17] The expansion of the tissue has enabled high-throughput testing with biobanking for colorectal,[18] breast,[19] and ovarian tumors[20], and can reveal particular drugs that target key signaling in cancer cells of specific patients.[21] Unfortunately, this expansion feature compromises the TME, including the immune microenvironment, during the process of tissue growth in culture[15] – limiting the general relevance of PDOs and OOCs as models for immunotherapy, since many immunotherapy drugs act on the TME.[22–24] These limitations are a fundamental hurdle for the personalization of therapies which need to be customized to the unique TME of the patient,[25] and also for the development of combination immunotherapies, which often target the human TME.[26] The pace of progress in clinical studies puts an additional pressure to developing reliable, quick, and inexpensive drug efficacy tests; immunotherapy clinical trials, especially in combination with other therapies, are exponentially rising in number.[27] In sum, PDOs and OOCs allow for high-throughput drug tests, but fail to faithfully recapitulate the patient's TME.

In addition to PDOs and OOCs, several other functional approaches to microscale drug testing have been proposed, each with advantages and limitations. Implantable or needle microdelivery devices[28–30] locally deliver small doses of (up to 16) drugs to the tumor *in vivo,* with maximal preservation of the TME, but issues of tumor accessibility and patient safety limit their applicability. Microdissected tumors (µDTs), comprising precision-cut tumor slices (PCTS)[6,31–34] and *ex vivo* patient-derived explants (PDEs) or fragments (prepared by multiple manual cuts),[35–41] consist of pieces of tumor that are thin enough for diffusion alone to ensure their viability and thick enough to preserve the TME *in vitro*. The latter is a spheroid approach that has been used for decades to preserve the tumor and its TME (with its native immune cells) within manually-cut small (~1-3 mm-wide) pieces. µDTs have shown promise for the study of immunotherapy with checkpoint inhibitors, but at low throughput.[6,33,34,42–46] The tumor fragments are minced manually with a scalpel and have been grown in collagen gel either on Transwells[45,46] or in microchannels.[43,44] Astolfi et al. prepared ~420 µm-diam. cylindrical µDTs by punching cores from PDX tumor slices and manually loading them in microchannels with five traps each; the reproducible size of the µDTs allowed for a metabolite transport model.[47] The same group later found higher survival rates and lower degree of hypoxia in punched µDTs than in PCTS from ovarian and prostate cancer PDXs, indicating an inherent diffusive transport benefit in smaller, higher surface-to-volume ratio pieces.[11] In sum, previous µDT techniques have recapitulated the TME but have not allowed for higher-throughput testing and do not maximize the use of precious biopsy tissue (e.g. loss during core punching or during filtering with selection among randomly sized pieces).

Motivated by tumor scarcity (tumors average ~1 cm^3 at the time of intervention[48], with size at diagnosis decreasing due to improvements in early detection techniques[49]), we recently developed a straightforward microdissection technique based on a tissue chopper that mechanically cuts tumors into thousands of regularly-sized, cuboidal-shaped µDTs (referred to as "cuboids") in ~30 min.[50,51] Due to their small size, cuboids can be rapidly arrayed into multi-well plates using either a microfluidic platform (featuring 96 wells, with 4 cuboids/well)[51] or a custom robot (up to 384 wells, with a programmable number of cuboids/well).[52]

Here we characterize the retention and function of the native TME over several days in culture from mouse and human tumor cuboids and demonstrate their suitability as microscale cancer models that can

complement existing models. We evaluate the presence of immune cells, vasculature, and cytokine secretion. In addition to traditional tissue culture platforms, we utilize devices with microfluidic arrays that facilitate 3D imaging and analysis as well as drug testing (schematic in **Fig. 1**A). We measure traditional viability drug responses and probe deeper into drug responses by protein profiling of signaling pathways and by unbiased proteomics. In a single assay, proteomics provides a complex readout that encompasses molecular responses to drugs as well as profiling the TME, including immune cells and cytokines. These results support cuboids as a valuable live tumor model with a rich TME that supports a wide variety of analysis approaches for deep investigation of solid tumors in the context of their TME.

RESULTS

Evaluation of cuboids in culture

Our cuboid microdissection technique uses automated and precise cutting in a way that allows us to maximize the yield of similarly sized, TME-retaining microdissected tissues, according to a cubic power law arising from three orthogonal cuts. The technique simultaneously optimizes cuboid viability, cuboid uniformity, and cuboid number. Theoretically (if the blade were infinitely thin and did not cause tissue loss), an ideal 1 cm^3 cube of solid tumor would yield 25^3 = 15,625 400 µm-wide cuboids, or 40^3 = 64,000 250 µm-wide cuboids. In practice, depending on the tumor, from an irregular ~1 cm^3 tumor piece we obtain over a thousand ~400 µm-wide cuboids and thousands of ~250 µm-wide cuboids due to various losses in the cutting and filtering processes (amounting to >75% loss of the tumor mass), but the cubic power law still holds. Typically, we first prepare tumor slices either with a vibratome (250 or 400 µm) or with a tissue chopper (400 µm) from 6-cm tissue cores. By geometry, a 400-µm cuboid has ~4.1 times more volume (and thus TME) than a smaller 250-µm cuboid. From previous work by others on tumor spheroids, we inferred that larger cuboids would result in hypoxic cores.[53,54] For the experiments shown here with mouse cuboids, we used syngeneic mice (with intact immune systems) and produced breast cancer tumors derived from the Py8119 cell line grown subcutaneously or orthotopically in the mammary fat pad. For mouse cuboids, but not human cuboids, the cuboid shape changed from polygonal immediately after cutting, to a spheroid shape by the following day, presumably due to differences in ECM stiffness; to consistently refer to these tissues by how they originated, we term them "cuboids" even if their final shape is spheroidal.

To understand the effect of cuboid size on various baseline cuboid parameters, we compared two sizes of cuboids (250 or 400 µm) from mouse or human tumors (**Fig. 1**B).[50] Live/dead staining at day 3 (**Fig. 1**B,C) showed viability of ~90% for both sizes of cuboids. We approximated the cuboid sizes at day 3, when they were rounded, by a diameter estimated from their area from an image (**Fig. 1**C). Using a vibratome to precisely cut the tumor into well-defined slices as the first cut, the diameter for the 250-µm cuboids was 313 ± 48 µm (ave. ± S.D.), and for the 400-µm cuboids was 422 µm ± 58 µm. We chose to continue with the 400-µm cuboids as a compromise between representation of the TME and nutrient exchange. As seen in tumor slices before cutting into cuboids (**Fig. 1**B,D), the patient tumors (colorectal cancer metastatic to the liver, CRClm) had more heterogeneity than the mouse syngeneic breast cancer model, with non-tumor stromal regions and necrotic bloody regions.

Mouse cuboid TME

As tumor explants grow in culture, the cellular makeup of the TME changes over time, presumably from cell growth, cell migration, phenotype alterations, and/or cell death.[6] We evaluated how the TME of Py8119 mouse breast cancer cuboids evolved over a week in culture. We focused on the first week in culture because this period provides a sufficient timeframe for functional assays and minimizes the time over which the TME has changed in culture. To evaluate the TME at a cellular level, we performed multi-immunohistochemistry (multi-IHC) on thin sections of 400-µm cuboids cultured in suspension in well

plates up to a week in culture (**Fig. 2**A), with quantitation by HALO (**Fig. 2**B). Comparison of day 0 to day 3 in culture showed general maintenance of tissue structure by H&E, followed by shrinkage of the cuboids by day 7, potentially secondary to apoptosis of the central core. Apoptotic cell death (cleaved-caspase 3, CC3) was minimal initially, limited to necrotic regions from the initial tumor seen at day 0, a few scattered cells the subsequent days, and often in the central region at day 3 (~10% of the cells), and decreased in the smaller sized cuboids of day 7. Proliferation (Ki-67) started very high initially, with ~50% of cells at day 0 and 45% at day 1, gradually reduced to ~25% at day 3, but persisted with ~10% of cells at day 7. Endothelial cell staining (CD31) gradually diminished from ~0.4% of the total area at day 0, to half at day 3, then to minimal staining at day 7. This rapid disappearance of vascular structures *ex vivo* is a common observation in explants and is likely due to apoptosis in the absence of circulation. Staining for immune cells (CD45) was strong initially then gradually diminished, persisted at reasonably high levels (unlike endothelial cells) and was variable between tumors, ranging from 10-60% of the cells at day 0. On average, we observed that CD45+ cells comprised 30% of all cells in both tumors and cuboids, which is consistent with the previously reported CD45+ fraction in PY8119 tumors.[31,55] As we saw similar staining in Py8119 tumors grown subcutaneously or orthotopically in the mammary fat pad (n=2 and 3, respectively), their data was combined in the graphs (**Fig. 2**B).

To look at specific immune cell types present in the cultured cuboids, we performed an additional 5-plex multi-IHC of near-adjacent cuboid sections (**Fig. 1**E,F). Like in Py8119 slices in culture by flow analysis,[31] we found that tumor-associated macrophage (TAMs) were the most frequent, comprising ~10% of the total cells in the cuboids throughout the week in culture, consistent with previous study of *in vivo* tumors.[55] There were also many tumor-associated neutrophils (Lys6G), though with weaker staining. We also observed scattered T cells (CD3) including some CD8+ T cells. We did not see many natural killer cells (NKp46) in the cuboids, which is consistent with the few clusters of positive cells seen in sections of the initial tumor. With multi-IHC we quantitated the average amount of immune cells (CD45), immune cell subtypes (CD3, CD8+, NKp46, Lys6G, TAMs), and endothelial cells for single 2D planes of groups of multiple cuboids. We did not perform analysis of rarer cell types for individual cuboids given the scarcity of sampling per cuboid and the small size of cuboids. Despite these limitations, the immunostaining clearly revealed the continued complexity of the cellular TME in cuboids over short-term culture.

To look at the effect of size on the TME of cuboids in culture, we also characterized 250 µm cuboids from two tumors by histology and multi-IHC. We found similar trends (**Fig. S1**), with a few key exceptions. There was much less apoptosis, as would be expected from their smaller size and the resulting better diffusive transport of nutrients and oxygen compared to 400-µm cuboids. There also appeared to be less retention of immune cells, as evidenced by the general immune marker (CD45), as well as macrophage and T cell markers. Further experiments could better characterize these changes. However, an overall decrease could reflect less retention of factors favorable to retention of cells, *i.e.*, preventing migration away and/or cell death.

Distribution of immune and endothelial cells by 3D immunostaining of mouse cuboids

To directly evaluate the distribution and heterogeneity of immune and endothelial cells among individual cuboids, we performed 3D immunostaining and analysis of intact mouse Py8119 cuboids (**Fig. 2**C-H). We used microfluidic devices with arrays of hydrodynamic cuboid traps (**Fig. S3**), similar to a device we developed previously for drug testing,[51] but without valves and with rapid fabrication by laser micromachining. Here, the device facilitated culture, immunostaining, clearing, and confocal analysis of the cuboids. The small microfluidic device contained 3 independent, rectangular wells, each with one outlet connected to 48 microtraps (144 traps total) (**Fig. 2**C,D). To load the device, we used flow (200 mL/hr suction) to pull cuboids into the traps. Suspension of cuboids in viscous 20% PEG facilitated the movement of the cuboids and minimized settling. To fill the device, one well at a time we gently pushed

the cuboids with a plastic "comb" across the surface and above the traps while we applied suction. The loading of each well (48 traps) with 1-3 cuboids per trap took approximately one minute. The cuboids were then cultured, fixed, immunostained, optically cleared, and imaged by confocal while remaining on the device. We evaluated cuboids derived from both subcutaneous and orthotopic (mammary fat pad injection) tumors.

To visualize the immune cells (CD45) and endothelial cells (CD31), we immunostained the cuboids at day 0 and at day 2 (**Fig. 2**D-F). 3D visualization and analysis of immunostained surfaces with Imaris revealed abundant CD45 cells at both time points, though less at day 2, and a more dramatic reduction in CD31 vasculature at day 2 (**Fig. 2**F). Quantitation of the amount of endothelial CD31 (**Fig. 2**G,H) showed an increase in variability between cuboids from day 0 to day 2, with most of the decrease in CD31 staining occurring in the larger cuboids. In contrast, although there was an overall decrease in the amount of immune cell CD45 staining at day 2, there was not a difference based on cuboid size. Unlike with the single cross-sections used for multi-IHC above where we could not differentiate between a central section of a small cuboid or a section off-center from a larger one, 3D immunostaining of intact cuboids allowed us to detect the relationship of endothelial cell staining retention at day 2 with smaller size.

Patient cuboid heterogeneity

We also looked at cuboids derived from patient tumors. In contrast to the relatively homogeneous mouse tumor models such as the Py8119 breast cancer tumors above, patient tumors are known to display large amounts of heterogeneity, both within tumors and between tumors of the same type.[31] Importantly, while many cuboids are required per condition because of patient tumor heterogeneity, analysis of individual cuboids enables direct assessment of the heterogeneity of patient tumor responses. We looked at the baseline heterogeneity in untreated patient liver tumors (**Fig. 1**D & **Fig. S2**), both colorectal cancer liver metastases (CRClm) and a primary liver cancer, idiopathic cholangiocarcinoma (ICC). We saw great variability in histology (H&E) of the cuboids and the initial tumor, and in viability (RealTime-Glo luminescence, RTG) of cultured cuboids (**Fig. S2**). The tumor exhibited regions of different colorations depending on the type of illumination. Some regions looked lighter with top-illumination, dark with through-illumination, and brighter with green autofluorescence. Also visible were regions with blood that were red with top-illumination, dark with through-illumination, and very dark with green autofluorescence. We had previously found that, in CRClm, regions of autofluorescence and darkness on bright-field images corresponded to relatively acellular stromal regions, presumably due to post-necrotic fibrosis after neoadjuvant treatment.[6] We measured viability by RTG luminescence after one day and saw a correlation between the RTG features and the autofluorescent stroma features. In cuboids from another patient CRClm (cultured in collagen with an air-liquid interface), we also saw a correlation between low RTG viability and stromal H&E histology (**Fig. S2**). These findings suggest that cuboids with low RTG viability are more likely to be predominantly stroma and not tumor cells, and underline the importance of tailoring applications to the particular type of tumor. Despite this complexity, our approach enables the direct assessment of individual cuboids, potentially facilitating the identification of specific tumor regions, such as stromal and bloody areas, through autofluorescence and viability measurements.

To further characterize the TME of patient cuboids in culture, we performed multi-IHC analysis of cuboids from two types of patient tumors: a CRClm and a metastatic melanoma from a lymph node (**Fig. 3**A,B). We looked at the initial tumor and 400-µm cuboids cultured for up to a week. Histology by H&E showed some remodeling, with qualitative maintenance of the tumor histology. In the CRClm, but not in the melanoma, from day 1 onward the tumor cells appeared to have formed a superficial layer in addition to tumor cells inside, potentially due to access to nutrients. In both tumors, despite scattered baseline apoptosis (CC3), we did not observe central apoptosis as we had observed in mouse. Though we could have missed the appropriate time point to catch central necrosis, the relatively consistent size of cuboids

over the week suggests that central necrosis had not occurred. Furthermore, we did not observe a marked decrease in cuboid size over time, as we had in the day 7 400-µm mouse cuboids, which had clearly undergone central necrosis at day 3 (**Fig. 2**A). In the patient cuboids we saw abundant proliferation (Ki67) at all timepoints, primarily in tumor regions as identified by histology (H&E or DAPI) and by tumor cell markers (partial staining of tumor cells: AE1/2 for CRC and a mix of markers for melanoma).

We then looked at the distribution of individual cell types (**Fig. 3**A,B). In CRClm cuboids, we observed clear endothelial cell staining (CD31) that tapered off over time. In melanoma cuboids, we only observed strong endothelial staining in a restricted area of the initial tumor, with minimal staining in both day 0 and in cultured cuboids. In CRClm initial tumor and cuboids, tumor-associated fibroblast staining (by smooth muscle actin, SMA) clearly colocalized with the relatively acellular, non-tumor, stromal areas. In contrast, in melanoma tumor and cuboids, SMA staining appeared to demarcate smooth muscle cells that surrounded CD31-positive blood vessels. General staining for immune cells by CD45 mainly revealed the very uneven distribution of immune cells in the initial tumors and in the cuboids. We also looked at macrophage (CD68), T cells (CD3), and CD8+ T cells. In contrast to the Py8119 mouse breast cancer tumor staining which had a predominance of macrophage with few T cells, in the human tumors and cuboids we saw relatively few macrophage and many T cells. In the melanoma, we found that most of the T cells were CD8+, with very large numbers in some cuboids and few to none in others. The overall heterogeneity of the immune cell staining between cuboids suggests that individual cuboids could be very different from each other, notably in tumor content for CRClm and in immune cell content for the melanoma. The results in the CRClm cuboids were consistent with findings from a 25-plex multi-IHC study of the immune microenvironment in CRClm.[56] The melanoma cuboid staining and histology appeared to conform more to the melanoma tumor which had invaded the lymph node than to the normal morphology of a lymph node, though further immunostaining could better distinguish the components and structure of lymph nodes. In sum, immunostaining revealed that, over the week in culture, the patient cuboids maintained the tissue complexity and heterogeneity of the initial tumors, including continued cell proliferation and a diversity of cell types.

3D immunostaining of patient cuboids

We wished to more thoroughly investigate the spatial heterogeneity of patient tumor cuboids using whole, intact cuboids. Whole-mount pseudo-H&E staining of a CRClm biopsy and cuboid highlight the variability of the histology both at distant regions and within the dimension of a single cuboid (**Fig. 3**C). In 3D immunostaining experiments on patient cancer cuboids (**Fig. 3**D,E), we looked at immune cell (CD31) distribution as well as at apoptotic cell (cleaved-caspase 3, CC3) distribution, given the larger amount of starting cell death compared to mouse. We used cuboids from one CRClm tumor (day 0 only) and one idiopathic cholangiocarcinoma (ICC) tumor, a primary liver tumor (day 0 and day 4). We used the ICC cuboids in a microtrap device, processed either immediately after loading (day 0), or after 4 days in culture. This device had a single chamber with 96 traps and a single outlet. Given tissue scarcity, to ensure loading of one cuboid per trap we used manual guidance of individual cuboids (visualized with a microscope) in addition to hydrodynamic flow. For the ICC cuboids, we used RTG luminescence to measure confirm the viability of the cuboids (**Fig. S2**I,J).

The patient cuboids were markedly more heterogeneous than the mouse cuboids, including in the amount of tumor (regions with many nuclei) versus non-tumor tissue (regions with very few nuclei). In contrast with mouse cuboids that showed minimal initial cell death (after elimination of necrotic areas during preparation before slicing), patient cuboids displayed multiple regions of cell death even at day 0 (**Fig. 3**D,E); many cuboids had very few, well-spaced cells, likely consisting of mostly connective tissue. There was some increase in CC3+ apoptotic cell death at day 4 in the ICC cuboids. At day 0 for both tumors, the CD45+ immune cells were present variably and in clusters, as had been seen by multi-IHC for other tumors

(**Fig. 3**A,B). At day 4 in ICC cuboids, immune cells were still clearly present, though at a reduced amount (**Fig. 3**E). Taken together the immunostaining results reinforce the initial observation from histological sections that patient cuboids also have higher heterogeneity than mouse cuboids in tumor representation, immune cell distribution, and presence of dead cells prior to culture. This immunostaining also confirms at the whole cuboid level the continued presence of immune cells and other cell types in culture shown by 2D multi-IHC in other tumor types.

Immune cell cytokine and chemokine secretion in cuboids

To evaluate the functionality of the immune cells within the cultured cuboids, we measured cytokines/chemokines in mouse and human cuboids grown in U-bottom 96-well plates with multiple cuboids per well (**Fig. 4**). Luminex measurement revealed abundant expression of cytokines/chemokines in the supernatant of Py8119 breast cancer and human CRlm cuboids, with 31 of 32 detected for Py8119, and 29 of 38 for CRlm (**Fig. 4**A,B). For Py8119, expression of multiple molecules secreted by the innate immune system (e.g. G-CSF, IL-6, and TNFα) is consistent with the abundant macrophage seen in cuboids by immunostaining above. CXCL10 may be produced by monocytes, endothelial cells, and fibroblasts. The interferon-gamma (IFNγ) and IL-2 signal is consistent with the low presence of T cells in cuboids by immunostaining and previous study (ref above). Application of lipopolysaccharide (LPS) for 24 hours to stimulate the innate immune system led to the expected increases in inflammatory cytokines, IL-1α and TNFα, and chemokines CCL3, 4, and 5 (**Fig. 4**C). In CRlm cuboids, 24 of the cytokine/chemokines were present at >10 pg/mL. For the patient CRlm cuboids, we observed high levels of Activin A (276 pg/mL), CCL2 (15.6 pg/mL), CXCL7 (55 pg/mL), CXCL10 (173 pg/mL), MIF (178 pg/mL), and IL-8 (84 pg/mL). Interestingly, we also found high levels of Triggering receptor expressed on myeloid cells, Trem2 (~4189 pg/mL), CD147 (8553 pg/mL), CRP, C-reactive protein released by hepatocytes in response to inflammation (2841 pg/mL) (**Fig. 4**D). We observed at least 10 different cytokine/chemokines, supporting the presence of functional immune cells such as macrophage in the cuboids. CXCL-10 has been shown to be expressed by CRC tumor cells as well as by macrophage. IL-8 is a key pro-inflammatory pro-tumor chemokine produced by tumor cells and tumor-associated macrophage in CRC.[57] CCL2 and CCL5 can be produced by CRClm tumor cells themselves.[58] CCL18 is produced by macrophages and monocytes. These cytokines support the use of cuboids as a model system for CRClm that natively expresses cytokines/chemokines critical to the immunomodulatory crosstalk between tumor and immune cells.

Drug treatment of mouse cuboids

As a first demonstration of drug responses in mouse cuboids, we treated Py8119 cuboids from a subcutaneous mouse breast cancer with 2 drugs using a 24-well microdevice with 96 microfluidic traps, and one device per condition (**Fig. 5**A-H). Each microfluidic trap contained up to 3 cuboids, with 4 traps per well. We measured viability by RTG luminescence before and after 3 day treatment with the cytotoxic chemotherapy drug, cisplatin (CP); the non-specific protein kinase inhibitor, staurosporine (STS), as a positive control; or a no drug negative control. By immobilization of the cuboids in fixed and separated locations in an array, the device facilitated analysis of viability by luminescence for individual traps. We observed significant responses to both CP and STS. Similar responses were seen using a Py8119 tumor grown orthotopically, using a device with three regions of 48 traps each (**Fig. S4**). While these microfluidic devices do not allow for multiplexing the drug treatments (the wells are fluidically connected), we have demonstrated a valved 96-well version of these microtrap devices that allows for testing unique drugs in each well.[51] While the present viability readout does not have enough resolution to discern between the different cell types, future improvements in the technique might allow a simultaneous readout of the viability of non-cancerous cells, or treatment of normal tissue in parallel as an assessment of the toxicity of the treatment.

To look at the variability of the drug response at the level of individual cuboids, in parallel on the same tumor we tested individual cuboids, manually pipetted into a 384-well plate (**Fig. 5**I-L). As in the microdevice, we saw a strong decrease in viability (RTG) in response to CP and STS. We also saw an increase in cell death using SYTOX Green (SG), a green fluorescent cell death marker. Despite the relative homogeneity of the tumor, there was some heterogeneity in the viability before drug treatment and in the viability after culture for the control conditions. Using the standard deviation values observed from these drug treatments, power analysis estimated that to detect a 50% change, we would need at least 2 cuboids for SG and 5 for RTG, and to detect a 30% change, we would need 4 cuboids for SG and 12 cuboids for RTG. These experiments were performed on the relatively homogenous mouse Py8119 tumor, so we expect that the number of cuboids needed for each condition with more heterogeneous tumors, especially with human patient tumors, would be much greater.

Cuboid responses to kinase inhibitors and to checkpoint inhibition

To demonstrate the suitability of cuboids for drug screening, we tested a drug panel of kinase inhibitors on mouse Py8119 cuboids in a standard 96-well plate format (**Fig. 5**M). With a multi-pipettor, we manually pipetted a random number of cuboids into each well, which resulted in 2-6 cuboids per well. After measuring the pretreatment viability by RTG luminescence, we removed high and low luminescence outliers to reduce the variability of the starting condition. We measured the drug responses (post/pre) after 3 days of drug treatment, relative to the DMSO vehicle control. The relatively high concentration used (500 nM) may contribute to the responses to many of the tested drugs. The reproducibility of the responses for duplicate wells for Py8119 breast cancer cuboids for this experiment contrasts with the variability seen in the single cuboid experiments with the same tumor type. We attribute this difference to both the use of a pool of cuboids per well here, as well as to the exclusion of wells with unusually high or low pretreatment luminescence. Testing multiple cuboids per well appears to reduce noise and minimize reagent use, and thus would facilitate higher-throughput drug testing approaches.

No known somatic mutation predicts response to immunotherapy despite the billions of dollars spent on genetic tumor profiling,[1] so functional tests are critically needed to ascertain the efficacy and toxicity of potential immunotherapy treatments. Tumor cuboids, with their intact TME, are an ideal platform for testing TME-dependent immunotherapy drugs. As proof of concept, we applied the PD-1 checkpoint inhibitor to MC38 mouse colon cancer cuboids (**Fig. 5**N). Checkpoint inhibitors remove the suppression on CD8 T cells, permitting the T cells to attack and kill the target cancer cells. After four days exposure to PD-1 in comparison to IgG control, we saw both a decrease in viability of ~40%, as well as a ~2-fold increase in IFNγ, a sign of activation of the immune system. This simple test confirms that cuboids could be used as immunotherapy drug evaluation platforms in a variety of settings.

Drug evaluation with patient cuboids

One defining test of the clinical relevance of a cancer model is to provide data about the efficacy of existing drugs, such as for a personalized treatment. We performed experiments that evaluated drug responses in cuboids derived from two patient tumor biopsies removed during surgery (**Fig. 6**). These two tumors were the same tumors analyzed by multi-IHC in **Fig. 3**. The first set of experiments utilized CRClm cuboids (**Fig. 6**A-G). The patient had undergone chemotherapy prior to resection, including only one cycle with FOLFOX, a combination of folinic acid, 5-fluorouracil (5-FU), and oxaliplatin, because of side effects. As seen in tumor slices (**Fig. 1**D) and cuboids (**Fig. 3**A), the tumor had regions that correspond to relatively acellular stroma as described before,[6] likely due to post-treatment necrosis. We found that we could identify putative stromal cuboids by brighter autofluorescence in the green channel, and bloody cuboids (red in light) as relatively dark areas in the green channel (**Fig. 6**A). We note that the same regions may also contain tumor cell areas, as the slices and cuboids were regularly thick (400 µm), and they may be

quite interspersed, as seen on H&E (**Fig. 3**A). To facilitate the transfer of large numbers of individual cuboids, we used a custom robot[52] to pipet one cuboid per well of a 384 well plate. We measured viability (RTG) before drug application (day 2), then at different time points after 3 and 5 days of drug exposure. We treated cuboids with either the standard chemotherapy regimens FOLFOX or FOLFIRI (a combination of 5-FU and irinotecan), or staurosporine, or DMSO vehicle control, or a no drug control. As an additional cell death readout, we measured cell death with propidium iodide (PI), a red nuclear cell death indicator, at the end of the experiment after 5 days of drug exposure on day 7. Pretreatment viability was variable, but similar between the wells used for the different treatments (**Fig. S2**). We observed both a decrease in viability (RTG) and an increase in cell death (SG) at day 7 to FOLFOX, FOLFIRI, and STS, consistent with the patient's relative lack of prior exposure to FOLFOX and FOLFIRI, which are the first-line choices for treatment.[59] The small overall reductions in viability for FOLFOX (20%), FOLFIRI (24%), and the STS positive cell death control (30%), may reflect the heterogeneity of the cuboids. However, the responses were highly significant despite the clear heterogeneity in the baseline signal, in the changes to control and DMSO treatments over time, and in the drug responses.

In cuboids from the biopsy of metastatic melanoma in an inguinal lymph node, we looked at the differences between the use of single and multiple cuboids per well for drug tests (**Fig. 6**H-K). The patient was scheduled to have an iliac lymph node resection and TIL (tumor-infiltrating lymphocyte) therapy. The tumor had progressed after initial response to checkpoint inhibitors (anti-PD-1 and anti-CTLA-4). The month prior to surgery, brief treatment with binimetinib (a BRAF inhibitor) led to tumor response, but the treatment was discontinued 10 days prior to surgery due to side effects. Although BRAF was not mutated, the tumor was found to have VPS54:BRAF fusion, and BRAF inhibitors have been approved for clinical use in metastatic melanomas with BRAF overexpression.[60] Thus, we chose to test the patient cuboids with one of the clinically approved MEK inhibitor (cobimetinib), a downstream target in the RA/RAF/MEK cascade, in addition to the standard checkpoint inhibition therapy (PD-1). We manually transferred either 1 or 8 cuboids per well of a 96-well plate; the groups of 8 cuboids tend to form a monolayered clump at the bottom of the U-bottom well. Mean baseline viability signal (RTG) at day 1 (**Fig. 6**H,I) increased only 5-fold despite the 8-fold average mass increase from 1 to 8 cuboids per well. However, as expected, the variability in the baseline viability by RTG decreased with 8 cuboids per well, showing half the coefficient of variation (55% for one cuboid and 26% for 8). We applied the drugs at day 1 for 6 days. The treatments were an anti-PD-1 checkpoint inhibitor, its IgG control, cobimetinib (a MEK inhibitor), STS (a multi-kinase inhibitor used as a positive cell death control), or a no-drug control. While measurement of viability by RTG revealed no response to checkpoint inhibition, we saw a clear response to cobimetinib and STS by 3 days of treatment (**Fig. 6**J,K). The lack of response to anti-PD1 is consistent with the patient's loss of response to checkpoint inhibition before surgery. In contrast, the response to the MEK inhibitor cobimetinib is consistent with the tumor's sensitivity to treatment with binimetinib, also a BRAF inhibitor, before surgery. As would be expected, the cobimetinib response was more clearly seen with 8 cuboids per well, with less variability and more significance at the earlier time point. However, 1 cuboid per well showed a response with much less tissue, suggesting that the compromise of using less tissue, or less reagent, should be decided for each application, including the anticipated variability of the responses.

Proteomics of drug-treated mouse cuboids

Over the last decade and largely driven by the efforts of NCI's Clinical Proteomic Tumor Analysis Consortium (CPTAC), mass spectrometry (MS)-based proteomics has provided profound insights into the molecular mechanisms, diagnosis, prognosis, and treatment of various types of cancer.[61] Discovery proteomics pipelines can now achieve very high (femtomole) sensitivity and tackle low input samples, providing quantification for thousands of proteins for laser-microdissected samples,[62] individual organoids,[63] or even single cells.[64] However, the massive efforts by the CPTAC have been undertaken on

frozen samples and do not provide functional information on drug responses. Recently, the combination of proteomics with microdissection techniques or "microscaled proteomics"[65] has permitted evaluation of drug responses on sequential core needle biopsies pre- and post-treatment. Proteomics of large, drug-treated cultured explants (~1 mm^3) derived from patient prostate cancers helped reveal some of the underlying molecular and cellular changes underlying the drug response,[66] and suggest the power of application to even smaller tumor pieces such as cuboids.

To provide a deep molecular readout of both drug-induced changes and the state of the TME at once, we adapted a "microscaled proteomics" workflow to the analysis of cuboids (**Fig. 7**). We treated cuboids from Py8119 orthotopic mouse breast cancer tumors in 6 well plates for 3 days with several drugs including kinase inhibitors. Treatments included the drugs clinically used for cancer: cisplatin (100 µM), paclitaxel (a cytotoxic chemotherapy microtubule inhibitor; 10 µM), crenolanib (a PDGFR inhibitor; 0.5 µM), and regorafenib (a VEGFR inhibitor; 0.5 µM); as well as doramapimod (a pan p38 MAPK inhibitor used for some autoimmune diseases; 0.5 µM) and a DMSO (0.1%) vehicle control. We prepared samples from replicates of 4 cuboids each, including no treatment (day 4) and pretreatment (day 1) controls. The data independent acquisition (DIA) strategy consistently identified over 50,000 precursors and 4,000 proteins per sample across treatments using the equivalent of 1 cuboid per injection (**Fig. S5**A). The DIA strategy also afforded precise protein quantifications (median CV<10%) across drug treatments (**Fig. S5**B), which resulted in high Pearson correlations across the dataset (>0.95)**.**

Analysis of the expression of select cancer and TME-relevant proteins from day 1 cuboids demonstrated the ability of the one proteomics assay to reveal similar information as other assays such as immunostaining, viability, and cytokine, but with multiple types of markers at once (**Fig. 7**A,B). Among others, we saw multiple proteins involved in cytokine and chemokine activities (**Fig. 7**A) as well as several TME markers (**Fig. 7**B).[67] These TME markers included proliferation (Ki67) and apoptosis (CC3), key measures of drug response; AGRE1 (F4/80) and CD68, markers of macrophage; MRC1 (CD206), a marker of M2 macrophage; PTPRC (CD45) a general marker for immune cells; and VME (vimentin), a marker for tumor cells and the epithelial-mesenchymal transition. Although this approach does not have the cellular resolution of immunostaining or the sensitivity of Luminex cytokine measures, it can in one test evaluate death, proliferation, cell types, and signaling using many target proteins.

We also examined the effects of the different drugs on the cuboid proteome. Clustering analysis (**Fig. 7**E) and protein abundance Pearson correlations across replicates (**Fig. 7**C), revealed that cuboid proteomes undergo substantial and reproducible remodeling in response to drug treatments. Paclitaxel treatment seems to elicit the most dramatic proteome changes in cuboids as reflected by the cluster separation in the PCA analysis (**Fig. 7**E). Crenolib appeared to cause changes in the proteome relative to DMSO, but to a smaller extent. A closer look at the cytotoxic microtubule inhibitor Paclitaxel identified expected patterns of drug action, with decreased proteins related to actomyosin structural reorganization and upregulation of proteins related to activation of the innate immune system (**Fig. 7**D). Gene Ontolology enrichment analysis (**Fig. 7**F) of regulated genes between DMSO or Paclitaxel treated samples also identified additional significantly regulated biological processes.

Profiling changes in signaling pathways from drug treated mouse cuboids

Although unbiased protein analysis using mass spectrometry provides the unique capability to detect thousands of proteins within cuboids, detecting post-translational modifications in selected proteins or closely related proteins within a network can be challenging due to the low sample input. To overcome this limitation, we adapted the reverse phase protein (RPPA) assay. This technique utilizes extracts from cuboids and phospho-specific antibodies to detect changes in protein activity.[68] By applying RPPA, we can more accurately identify and quantify post-translational modifications and protein activity changes, even in low-abundance proteins, thus enhancing our understanding of protein dynamics within the TME. We

used reverse-phase protein array (RPPA) to look at dynamic changes in signaling pathways in mouse cuboids with drug treatment (**Fig. 8**). Py8119 breast cancer cuboids were probed with antibodies to look at the activity of 48 proteins, primarily by the phosphorylation state of kinases and kinase-associated proteins. Cuboids were treated with cisplatin (10 and 100 µM), doxorubicin (an anthracycline cytotoxic chemotherapy drug, 10 µM), staurosporine (2 µM), or DMSO vehicle control. Two samples of ~10 cuboids each were probed with 48 antibodies, and 23 yielded high-quality signals. The corresponding 23 proteins revealed distinct protein correlations, physical and predicted functional protein-protein interactions, and enriched biological processes from gene enrichment analysis. Six proteins of interest showed differences between drug treatments and DMSO (**Fig. 8**A,B). Phospho-histone H2A.X (P-H2A.X), a marker of DNA damage, is elevated in the drug treatments relative to controls, as expected. A dramatic reduction in phosphorylation of ERK signal was seen for all drug treatments. Reductions in phosphorylation of CREB, p-S6 ribosomal protein (S240/244) and p-Src family kinases (SFK) varied between drugs, with staurosporine and the higher cisplatin concentration causing greater decreases than doxorubicin or than the lower cisplatin concentration. Results from the 23 proteins of interest were used to create a Pearson correlation matrix and a protein-protein interaction network (**Fig. 8**C,D). Finally, gene enrichment analysis of the positively correlated proteins (**Fig. 8**E) yielded the top biological processes involved: regulation of apoptosis, transmembrane receptor protein tyrosine kinase signaling pathway, regulation of telomerase activity, and regulation of telomere maintenance. The network of proteins that were substantially downregulated in response to chemotherapy includes receptor tyrosine kinase, such as MET, cytosolic effector proteins like MEK, SRC, FAK, and S6, as well as cytoskeletal proteins such as RAC1. This is particularly interesting because PY8119 is a triple-negative breast cancer (TNBC) model known to be driven by the c-MET pathway. In the majority of TNBC tumors, c-MET is overexpressed, making it a critical driver of cancer progression in these models. The downregulation of these key proteins in response to chemotherapy suggests a potential mechanism by which the treatment exerts its effects and highlights the importance of the c-MET pathway in the pathology of triple-negative breast cancer. This insight could be valuable for developing targeted therapies aimed at inhibiting the c-MET pathway, potentially improving treatment outcomes for patients with TNBC. Overall, a combination of unbiased proteomics and focused PTM using RPPA can provide a rich, targeted analysis of dynamic changes in signaling pathways in cuboids in response to treatments. This integrated approach can yield valuable insights into the molecular mechanisms underlying treatment responses, potentially guiding the development of more effective therapeutic strategies.

DISCUSSION

Cuboid-based testing is complementary to other forms of current *ex-vivo* cancer drug tests. Compared to precision-cut tumor slices (PCTS), cuboids allow for much higher throughput in testing and benefit from additional surface-to-volume ratio for improved diffusive mass transport (which reduces hypoxia conditions).[11] A similar comparison applies to patient-derived explants (PDEs), which also suffer from low throughput and inconsistent sizing, but retain the TME like cuboids and PCTS. By comparison to (growth-based) organoid testing, which allows for high-throughput biobanking strategies but cannot address TME-dependent therapies, the intact TME of cuboids and their straightforward preparation in large numbers makes cuboids a suitable cancer disease model for performing TME-dependent drug evaluations of a small number of drugs. This number may be improved in the future thanks to the cubic power law governing the microdissection protocol. In principle, the microdissection process can be improved to yield more cuboids per unit volume using sharper and thinner blades. While the TME of a cuboid is more intact (and thus a closer biomimic) than that of an organoid, it is still not perfectly physiological. The TME did evolve in culture as evidenced by our immunostaining, and each cuboid lost its original metabolic microenvironment, including oxygen levels, normally lower than the tissue culture standard of 20%

oxygen used in our study. In principle, a more precise control of oxygen levels and metabolism can be achieved with specialized incubation and perfusion setups. Our microscale model presently does not incorporate functional vascular structures, so each cuboid relies on diffusive mass transport to deliver oxygen and nutrients to all their cells. While the absence of circulation imposes some limits on cuboids, the quantitative reproducibility of diffusive processes at small scales could be an invaluable experimental tool. The microscale size of spheroids, for example, has been used to control and recapitulate hypoxic gradients and necrosis.[69]

We demonstrated the suitability of cuboids for drug testing by evaluating the efficacy of 30 different drugs in PY8119 cuboids as well as of small panels of clinically relevant drugs in cuboids from two types of patient tumors. This evaluation confirmed that cuboids can effectively model tumor responses to various treatments. In combination with our low-cost, high-throughput robotic system, we have the capability to potentially test hundreds of drugs using tissue from a single surgical resection of a patient tumor. This approach not only enhances the efficiency of drug testing but also facilitates personalized medicine. Though we only looked at acute responses to drugs over several days, and tumor responses in patients occur over months, such studies could still provide critical insight into drug action in that particular tumor. By tailoring treatment strategies based on the specific responses observed in cuboids derived from individual patient tumors, we can potentially improve therapeutic outcomes and provide more precise and effective treatment options for cancer patients.

Given its breadth, flexibility, and sensitivity, MS-based proteomics promises to be very effective at evaluating intact-TME responses to drugs and modeling mechanisms of drug response and resistance.[65] MS-based proteomics is commonly regarded as an expensive technique that is not suitable for multi-well analysis, however isobaric labeling, *e.g.*, using Tandem Mass Tags (TMTs), a widely used technique for protein quantification by MS, offers the benefits of multiplexing and high throughput. TMT labeling allows for the simultaneous quantification of thousands of proteins across multiple samples in a single analysis[70] and has become the approach of choice by the CPTAC to characterize tumor proteomes.[71] Here we have used unbiased screening with discovery proteomics. Compared to discovery proteomics, targeted proteomics could possibly achieve even greater (attomole) sensitivity and precision quantification of subsets of proteins of interest,[72] markers of cell composition or immune response[73] and proteins in pathways relevant for tumor biology.[74] While immunohistochemical (IHC) imaging provides the ability to localize and detect very rare cells,[75] proteomics is complementary. Though it lacks spatial localization, proteomics offers superior and unbiased depth and quantitative capabilities. Targeted proteomics offers higher accuracy and precision than IHC imaging measurements, and for hundreds of proteins at once instead of a handful for IHC.[72,76] We conclude that the absence of collagen in our cuboid cultures facilitates the integration with proteomics, which allows for assaying the TME at high molecular depth, the biological changes underlying drug responses, and their heterogeneity.

CONCLUSIONS

Here we demonstrate that microdissected tumor "cuboids" from syngeneic mouse tumor models and human tumors retain a complex TME that makes them suitable as *ex vivo* cancer disease models for functional drug and immunotherapy evaluations that could complement existing cancer disease models based on PDXs, PDOs, and OOCs. Multi-IHC of mouse cuboids over a week in culture revealed continued proliferation and persistence of key cell types including immune cells. 3D immunostaining of endothelial and immune cells showed the heterogeneity of the cuboids. Cytokine secretion from mouse and human cuboids further supported the functionality of the immune cells in cuboids. Drug treatment of individual mouse and human cuboids demonstrated the amount of heterogeneity in the responses by both viability and cell death assays, while treatment of cuboids in groups facilitated testing a drug panel. We demonstrated the power of proteomic analysis of mouse cuboids to deeply analyze molecular changes in

response to drugs, as well as to reveal the presence and functional state of the TME. Finally, with RPPA on mouse cuboids we showed molecular profiling of the signaling pathways in response to drugs. Together, this data supports the potential for cuboids as a model system to help bridge the critical gap for cancer biology and cancer drug testing between organoids (which have high throughput and lack TME) and human patients. Cuboids offer higher throughput than patient slices, while preserving much of the TME, unlike organoids. Like spheroids, cuboids can be integrated with many modalities of assays,[77,78] which will allow researchers to tailor experiments with cuboids to help tackle outstanding problems in cancer biology and clinical oncology.

MATERIALS AND METHODS

Cell culture

The Py8119 syngeneic mouse breast adenocarcinoma cell line (American Type Culture Collection (ATCC), CRL 3278) was grown in DMEM/F12 (for subcutaneous injection) or F-12K (for orthotopic injection) supplemented with 5% FBS and 1% penicillin/streptomycin. The MC38 syngeneic mouse colon carcinoma cell line (Kerafast, ENH204-FP) was cultured in DMEM supplemented with 10% FBS and 1% penicillin/streptomycin. Tissue culture reagents were obtained from GIBCO, ATCC, or Fisher.

Tumor generation for mouse model

Mice were handled in accordance with institutional guidelines and under protocols approved by the Animal Care and Use Committee at the University of Washington, Seattle or by the Fred Hutchinson Cancer Research Center. Mouse syngeneic tumor cell lines (Py8119 and MC38) were injected into C57BL mice (Jackson Laboratories), >6 week old female (Py8119) or male (MC38) mice. 1-2 x 10^6 cells were injected subcutaneously (both lines) or orthotopically in Matrigel (Py8119, Corning). Tumors were harvested at < 2 cm^3. If not used immediately, the tumor was stored up to overnight in Belzer-UW cold storage medium (Bridge-to-Life Ltd).

Human tissue

Human tissue was obtained with written informed consent and treated in accordance with Institutional Review Board approved protocols at the University of Washington, Seattle. Tumors were processed for slicing the same day as the resection. For 2D immunostaining and viability measures as well as pseudo-H&E of a needle biopsy, we used a biopsy from a 40 year-old male with metastatic colorectal carcinoma to the liver, responsive to neoadjuvant treatment. Slices were cultured overnight after the biopsy and made into cuboids (considered as day 0). Cuboids were grown in 1 mL of collagen on a Transwell with an air liquid interface and analyzed for viability and drug response using RealTime-Glo (Promega), followed by immunostaining. For pseudo-H&E on cuboids, we used a biopsy of the liver metastasis from a 66 year-old female with untreated cecal adenocarcinoma. For 3D immunostaining, we used a biopsy from a 43 year-old male with colorectal carcinoma metastatic to the liver, after being off chemotherapy for a year. Cuboids were cultured in a 96 well plate, followed by immunostaining and imaging in the microfluidic device. For 3D immunostaining, we used a biopsy from a 70 year-old female with untreated intrahepatic cholangiocarcinoma. Cuboids were cultured in microwell devices, followed by immunostaining and imaging in the device. For multi-IHC and drug testing of a CRClm, we used a biopsy from a 29 year-old female with rectal cancer with recurrent metastasis to the liver, after initial treatment with CAPOX (capecitabine and oxaliplatin) followed by only one cycle of FOLFOX 2 months. Slices were cultured overnight and cuboids were prepared the following day. Cuboids were either grown in a 6-well plate for multi-IHC, or placed individually into a 384-well plate for drug treatment using a custom pipetting robot.[52] Also for multi-IHC and drug testing, we used an inguinal node biopsy from a 38 year-old female with widely metastatic melanoma that had progressed after initial response to checkpoint inhibition. The tumor did

not have a BRAF mutation but had VPS54:BRAF fusion. Cuboids cut from patient slices were manually pipetted into a U bottom 96 well plate at 1 or 8 cuboids per well for drug treatment. Cuboids were also cultured in a 6 well plate for immunostaining.

Cuboid generation and culture

After removing necrotic region from the tumors, we generated cuboids as previously described.[50] For human tumors, and if specified for mouse tumors, slices were cut using a Leica VT 1200 S vibrating microtome or MZ5100 vibratome (Lafayette Instruments) after embedding tissue punches (6 mm diameter, Harris Uni-Core) in 1-2% low-melt agarose. Otherwise, we cut small pieces of tissue into slices using a tissue chopper (McIlwain) after attaching the tissue to the plastic disk with cyanoacrylate glue. We cut slices into cuboids with the tissue chopper, then gently dissociated the cuboids with a transfer pipette. The tissue chopper can be used for all three cuts in sequence (including the first cut) to reduce the duration of the procedure, but at the cost of higher variability in cuboid sizes. For 400-µm mouse cuboids, we filtered them for size less than a 750 µm filter and greater than a 300 µm filter (Pluriselect). To further remove potential contamination, we transferred the cuboids to a 100 µm cell strainer (Corning or Falcon) and passed them twice through sterile PBS and once with medium. For the scarce human tumors, we did these washes in sterile tubes instead. For CRClm and ICC human cuboids, MC38 mouse cuboids, and Py8119 cuboids (cytokine, checkpoint inhibitor, and drug panel experiments), the culture medium was HFH: Williams' Media E (Sigma) supplemented with nicotinamide (12 mM), L- ascorbic acid 2-phosphate (50 mg/mL), D-(+)-glucose (5 mg/mL) from Sigma; sodium bicarbonate (2.5%), HEPES (20 mM), sodium pyruvate (1 mM), Glutamax (1%), and penicillin–streptomycin (0.4%) from Gibco; and ITS + Premix (1%) and human EGF (20 ng/mL) from BD Biosciences. For other Py8119 experiments (e.g. immunostaining, RPPA, and proteomics), cuboid culture medium was DMEM/F12 with 5% heat-inactivated fetal bovine serum , penicillin-streptomycin (0.1%). One human colorectal cancer tumor (**Fig. S2**A-H) was cultured in 1 mL collagen on top of a 0.4 µm filter Transwell PFTE membrane insert (PICMORG50, Millipore) in 6 well plates, with 1.3 mL culture medium placed below. We prepared 80% collagen (Corning rat tail collagen type 1, 354236, 3-4 mg/mL) with 10 % 10x PBS, and 10% serum-free medium. We then used filtered-sterilized 1M NaOH to neutralize the pH to ~7.2. For the CRClm drug testing experiment, cuboids were transferred individually to a 384-well plate using a custom robotic platform for cuboid manipulation[52] from a dish containing medium plus 1% bovine serum albumin (Sigma ro Rockland).

Drug treatment and functional assays of cuboids

To measure viability, RealTime-Glo (Promega) was added at 1x or 0.5x and after overnight incubation, the baseline luminescence was read by IVIS (Perkin-Elmer). Drug was added to the well, and luminescence was read again after incubation with drug without further addition of RealTime-Glo. To measure cell death as an endpoint, SYTOX green (1/50,000; Invitrogen) or propidium iodide (1 µg/mL), and/or Hoechst (16 µM, Invitrogen) were added to the well, incubated 1 hr at 37°C, then imaged with or without washing twice in PBS. For drug panel experiments, multiple cuboids were randomly distributed by manual pipetting, and baseline viability was used to remove outliers before randomly assigning treatments. Cytokine measurements were performed with Luminex.

Cuboids were treated with lipopolysaccharide (Sigma L4516) or drugs. Antibodies to checkpoint inhibitors (10 µg/mL) were human anti PD-L1 antibody (Bioxcell, BE0285; or BD Biosciences, 562138), mouse anti-PD-L1 antibody (Bioxcell, BE0101; or Leinco Technologies, P372), and mouse IgG control (Leinco Technologies, R1367). Drugs for treatment of cuboids included cisplatin (MedChemExpress), staurosporine (Thermo Scientific), and fluorouracil, oxaliplatin, irinotecan, and cobimetinib (Selleck).

The 35 drug panel for treatment of Py8119 cuboids, in order, was DMSO, Baricitinib (LY3009104, INCB028050), Doramapimod, JNK Inhibitor VIII, TCS ERK 11e (ERK Inhibitor VIII, VX-11e), Rho Kinase

Inhibitor III Rockout, PP121, GZD824, Staurosporine, AZD3463, NVP-BVU972, Y-39983 dihydrochloride, cobimetinib, WZ3146, Aminopurvalanol A, SB202190 (FHPI), PD 166285 dihydrochloride, BIIB-057 (PRT062607, P505-15), Akt Inhibitor VIII Isozyme Selective Akti-1/2, CP 547,632, Bosutinib, AT7867, Cdk1/2 Inhibitor III, PDK1/Akt/Flt Dual Pathway Inhibitor, SB 218078, PF-3644022, LY 333531 mesylate (Ruboxistaurin), Cot inhibitor-2, PD 173955 Analogue 1, Vargatef (Nintedanib), BIBF 1120), K252a, Nilotinib, GSK650, Regorafenib, Pazopanib, and At9283. Drugs were obtained from MedChemExpress, Selleckchem, TOCRIS, Cayman, and Sigma.

Microfluidic device fabrication and use

Microchannels were made in a process adapted from Horowitz et al.[50] We designed the devices in AutoCAD (Autodesk), and then fabricated them by laser micromachining (VLS3.60, Scottsdale, USA) of PMMA substrates followed by thermal solvent bonding and adhesive bonding. The device has four layers. The 800 µm-thick PMMA channel network layer (Clarex, Astra Products) has laser-cut microchannels that connect the outflow channel(s) to microtraps via binaries. The microtraps were approximately 560 µm in diameter at the top and 620 µm at the bottom. The microchannels were approximately 410 µm wide except for near the traps where they were approximately 320 µm wide. After sonication of the microchannel layer in isopropanol for 1 min, we bonded it to a 300 µm-thick PMMA sealing layer (Clarex, Astra Products) using thermal solvent bonding; we exposed both layers to chloroform vapor (~3 mm above the liquid) for 4 min, manually pressed them together, then sealed in a heat press for 5 min at 140 °C, 240-260 psi. The well plate layer was laser-cut from 6.35 mm-thick PMMA (1227T569, McMaster-Carr, Elmhurst, IL) and bonded to the channel layer using double-sided 3M™ High-Strength Acrylic Adhesive 300LSE for 2 min at 250 psi in the thermal press. Silicone tubing was bonded to the outlets using cyanoacrylate glue. Optionally, an additional well plate layer was hand-bonded onto the device after cuboid loading using the 300 LSE. The devices were sterilized by running 70% ethanol through the channels.

To load cuboids into the devices, cuboids were suspended in ice cold 20% polyethylene glycol (8k-PEG P2139, Sigma-Aldrich) and pipetted into the well. Suction was applied with a 60 cc syringe and a syringe pump (Chemyx Inc.) at 200 mL/hr for 96-microtrap wells or 100 mL/hr for 48-microtrap wells. Mouse cuboids were pushed around the well slowly using either a custom window (single-well, 96-trap device), or a comb (3 well device). For the scarce human cuboids, under visualization with a VHX-970F microscope (Keyence), cuboids were pushed manually to the vicinity of the traps using forceps to encourage only one cuboid per trap. More PEG and more cuboids were loaded as needed. The loading process took about 10 min for the 96-trap wells and 1 min for each 48-trap well. The device was placed into a 10 cm petri dish for culture.

Immunostaining and histology

For multi-immunohistochemistry experiments, tissue pieces and cuboids were fixed in 4% paraformaldehyde and washed with PBS. Cuboids were then embedded in Histogel (Epredia) plugs. Tissue was then processed for microarrays, paraffin sectioning, hematoxylin & eosin (H&E) staining, and multi-immunohistochemistry (multi-IHC) by the Experimental Histopathology Service at the Fred Hutchinson Cancer Research Center. Paraffin section (4 µm) were stained using the Leica BOND Rx stainer and processed with either two 5-plex (mouse) or three 3-plex (human) stains. Lists of antibodies are given in the supplemental materials. Staining for tumor cells (CK19) was weak and variable so was not used for quantitation. DAPI was used as a nuclear counterstain.

For peroxidase immunostaining (**Fig. S1**), tissue was fixed in 4% paraformaldehyde overnight then cryoprotected with 30% sucrose/PBS overnight two times. Cryosections (14 µm thickness) were then processed for H&E or for immunostaining. For immunostaining, we pretreated with 0.6% hydrogen

peroxide in methanol for 30 min, washed, and then performed antigen retrieval by steaming for 30 min in 10 mM sodium citrate, 0.05% Tween 20 (Sigma), pH 6.0. After at least 30-min block in blocking solution (Tris-NaCl-blocking buffer or TNB buffer, Perkin Elmer, with 0.1% Triton X-100), we incubated the tissues with rabbit primary antibodies (diluted in TNB) overnight at 4 °C. Antibodies were: active cleaved caspase 3 (1/600, Cell Signaling), Ki-67 (1/1,000, AbCAM, ab15580), CD31 (1/200, AbCAM ab28364), or CD45 (1/1,000, AbCAM, ab10558). After incubation of the tissues with an anti-rabbit peroxidase polymer (Vector Labs MP7401) for 30 min, we visualized the staining with 3,3'-Diaminobenzidine (DAB, Vector Labs) and a light hematoxylin counterstain. Washes between steps were done with PBS except for just before DAB incubation, done with 10 mM Tris pH 7.5.

We performed whole mount immunostaining in the microfluidic devices with a protocol adapted from Li et al.[79] Cuboids were incubated in block (PBS + 0.3% Triton + 1% BSA + 1% normal mouse serum) for >12 hrs at 37 °C on a shaker, then in primary antibody diluted in block for 2 days at 37 °C on a shaker. Primary antibodies were Alexa 647 anti-mouse CD45 (1:200; Biolegend), Alexa 488 anti-mouse CD31 (1:250; Biolegend), Alexa 647 anti-human CD45 (1:400; HI30 Biolegend 304056), rabbit anti-human/mouse cleaved-caspase 3 (1:300; Cell Signaling, 9661), followed by 1:500 546-Donkey/Goat anti-rabbit (or other). We then washed the cuboids 3 times with PBS at least 8 hrs total at 37 °C on a shaker. For the unlabeled primary we incubated with Alexa 546 donkey anti-rabbit IgG (1:500; Invitrogen) diluted in block for 2 days at 37 °C on a shaker followed by washing as above. DAPI 1 µg/mL was added to the last antibody step. We then cleared the tissue by incubation in previously prepared Ce3D solution overnight at room temperature with shaking. The day 0 human ICC cuboids were immunostained in a centrifuge tube and imaged in a custom well.

Pseudo-H&E staining (TO-PRO-3 and eosin, ethyl cinnamate clearing) and open-top light-sheet microscopy of a needle biopsy and cuboids (embedded in low-melt agarose) were performed by Alpenglow Biosciences, Inc., with methods like those described previously.[50]

Imaging and image analysis

We took images using a Canon DS126601 on a Nikon SMZ1000 dissecting scope, a Nikon Eclipse Ti microscope, a BZ-X800 (Keyence) microscope, or a Leica SP8 confocal microscope (10x, 2 µm Z steps, at the Lynn & Mike Garvey Imaging Core at the University of Washington). For confocal imaging of 3D immunostaining, we only imaged cuboids at the bottom of a well. For general image manipulation we used FIJI.[80]

Multi-IHC imaging utilized the Vectra Polaris Quantitative Pathology Imaging System (Akoya Biosciences, Marlborough, MA). Images were spectrally unmixed using Phenoptics inForm software and exported as multi-image TIF files. For multi-IHC image analysis, we used HALO and HALO Link (Indica Labs). For cellular analyses, cells were identified by nuclear DAPI stain, then cytoplasmic boundaries were drawn. For antibodies with clear staining, we applied the same settings to all tissues (Ki-67, CD45, CD3, CD8, and F4/80). For NKp46 which had few cells in cuboids d1-d7 with high background, we did a manual count. For Ly6G, we used one setting for strong staining and another for the groups of cuboids with high background. For area analyses, we applied the same settings to all tissues of that tumor type. We used the background staining from CK19 or from NKp46 to determine the total tissue area.

For 3D image analysis, we used Imaris (Oxford Instruments) through the Lynn & Mike Garvey Imaging Core. Cuboid volume was determined by creating a surface with the DAPI channel or background from another channel. CD31 and CD45 surfaces were created using Labkit for machine learning. For CD31, we applied a gaussian blur before further analysis. We trained the classifiers for d0 and d2 separately on a stack of two cuboids initially then applied the classifier to all of the cuboids in that day's group. For CD45 on mouse, we trained the classifier on day 0 then applied those settings to all of the cuboids.

Statistical analysis

Graphpad Prism 7 was used for statistics unless otherwise noted. Post-hoc power analysis was performed using https://clincalc.com/stats/samplesize.aspx.

RPPA

Protein microarrays were printed and processed as previously described.[68] Briefly, cuboid lysates (duplicates of 10 cuboids/sample) from the PY8119 syngeneic mouse breast adenocarcinoma cell line were prepared in 2% SDS lysis buffer (stock recipe (pH = 6.8): Tris·HCl 50 mM, 2% SDS, 5% glycerol, EDTA 5 mM, and NaF 1 mM. Immediately before use, we added protease inhibitors and phosphatase inhibitors (β-GP 10mM, PMSF 1 mM, Na_3VO_4 1 mM, and DTT 1 mM) and then printed onto RPPA slides, each containing 16 nitrocellulose pads (Grace Biolabs, GBL505116), using Aushon 2470 microarrayer (Aushon BioSystems). Samples were printed in duplicate and stored at −20 °C until processing. Slides were then washed with 1 M Tris·HCl (pH 9.0) for 2 to 3 days to remove SDS and PBS solution for 10 to 15 min, centrifuged with Thermo Sorvall Legend XTR Refrigerated Centrifuge (Thermo Scientific), and scanned with InnoScan 910 AL (Innopsys) to ensure no residual SDS. Slides were washed with PBS solution 2 to 3 times for 5 min each and then blocked with Odyssey blocking buffer (OBB) (Licor, 927–40000) for 1 hr at room temperature. Afterwards, slides were fitted to hybridization chamber cassettes (Gel Company, AHF16), incubated with primary antibodies on a shaker overnight at 4 °C. The following day, slides were washed with PBS thrice for 10 min each, blocked again with Odyssey blocking buffer (OBB) (Licor, 927–40000), and incubated with IRDye-labeled secondary antibodies for 1 hr at room temperature. After incubation, slides were washed in PBS 3 times for 10 min each, centrifuged again with Thermo Sorvall Legend XTR Refrigerated Centrifuge (Thermo Scientific), and scanned using Licor Odyssey CLx Scanner (LiCOR). Total signal intensity was normalized to total beta-actin (Sigma, Catalogue No A1978) and quantified using Array-Pro analyzer software package (Media Cybernetics, Maryland, USA).

Cuboid sample preparation for mass spectrometry analysis

4 PBS washed cuboids per replicate were resuspended in 40 µL of lysis buffer (6M GuHCL, 50 mM Tris pH 8.2, 75 mM NaCl, 10 mM TCEP, 30 mM CAA). The cuboid suspension was subjected to 4 rounds of agitation at 90 °C for 5 min followed by 15 min of bath sonication at 40 °C. Alkylation was quenched with 15 mM DTT for 30 min at room temperature and the samples were diluted 5-fold with Tris 50 mM pH 8.9 prior to digestion, which was carried out overnight at 37 °C using LysC at a 5 ng/µL concentration. Digestion was quenched with 1% TFA prior to desalting with oasis prime HLB µElution (Waters). Desalted peptides were dried down by vacuum centrifugation.

Mass spectrometry data acquisition

Lyophilized peptide samples were resuspended in 3% ACN, 5% formic acid and subjected to liquid chromatography coupled to tandem mass spectrometry (LC-MS/MS). Samples were loaded into a 100 µm ID x 3 cm precolumn packed with Reprosil C18 1.9 µm, 120 Å particles (Dr. Maisch). Peptides were eluted over a 100 µm inner diam. (I.D.) x 30 cm analytical column packed with the same material housed in a column heater set to 50 °C and separated by gradient elution of 6 to 38% B (A: 0.15% FA , B: ACN 80% and 0.15% FA) over 65 min and 38% to 50% B over 8 min at 400 nL/min delivered by an Easy1200 nLC system (Thermo Fisher Scientific) with a total 90 min method length. Peptides were online analyzed on an Orbitrap Eclipse Tribrid mass spectrometer (Thermo Fisher Scientific). Mass spectra were collected using a data-independent acquisition method. For each cycle a full MS scan (358-1100 m/z, resolution 60,000, and Standard 100% normalized AGC target in automatic maximum injection time mode) followed by 30 consecutive non-overlapping MS/MS scans with 24 m/z wide isolation windows. MS/MS scans were acquired at 30,000 resolution in centroid mode, using HCD fragmentation with 33% normalized collision

energy and an 800% normalized AGC target with automatic maximum injection time mode. In alternating cycles, the mass target list for MS/MS scans was offset by 12 m/z to produce DIA windows with half overlap spanning the 363-1095 m/z mass range.

Mass spectrometry Data Analysis

Raw files were converted to mzML format and demultiplexed using MSConvert followed by analysis with FragPipe (version 19.1) proteomics pipeline. Searches were performed with MSFragger (version 3.7) using a target/decoy *Mus Musculus* database (Uniprot fasta proteome: UP000000589_2023-03-02). Search parameters were set to 20 ppm for both precursor and fragment tolerances. LysC was selected as the digestive enzyme with a maximum of 1 missed cleavage and fixed constant carbamidomethylation modification of cysteines (+57.0215 Da) and variable modifications of methionine oxidation (+15.9949 Da) and protein N-terminal acetylation (+42.0106 Da). Search results were post-processed with Philosopher (version 4.8.1) using Percolator (3.05) filter the results to 1% FDR and ProteinProphet for protein inference. EasyPQP was used to generate a peptide spectral library and quantification was carried out using DIA-NN 1.8.2.

Bioinformatic analysis was performed using R (https://www.r-project.org/) and the R Studio environment. MSStats (version 4.01) was used to parse DIA-NN quantification outputs, generate and normalize protein quantification and carry out statistical significance analysis. Gene ontology enrichment analysis was carried out using CusterProfiler.

Author contributions

Conceptualize: LFH, RR, JV, TSG, AF
Methodology: LFH, RR, JV, TG, AF
Performed experiments: LFH, RR, MC, SZ, NRG, IS, TNHN, EJL, TSG
Supervision: RSY, JV, TSG, AF
Visualization and analysis: LFH, RR, SZ, CS, MY
Writing: LFH, RR, JV, TSG, AF

Data availability

Multi-IHC images and 3D imaging data and analysis is available on reasonable request. Proteomics and RPPA data.

Conflicts of interest

L.F.H. and A.F. are the founders of OncoFluidics, a startup that seeks to commercialize drug tests using intact tissues and microfluidic technology. L.H and A.F. are inventors in U.S. patent No. US 9,518,977 (filed 13 Dec 2016) and US patent applications No. 63/428,542 (filed 29 Nov 2022) and No. 18/652334 (filed 1 May 2024) related to this work.

Acknowledgements

This work was supported by National Cancer Institute grants R21CA251952, R01 CA181445, and R01 CA272677. R.A.R and J.V. received funding from a NIGMS grant R35GM119536, a NHGRI grant RM1HG010461, and from UW Bridge Funding. This research was supported by the Experimental Histopathology Shared Resource of the Fred Hutch/University of Washington Cancer Consortium (P30 CA015704). We thank Heidi Kenerson for preparation of human slices.

REFERENCES

1. Mellman, I. *et al.* De-Risking Immunotherapy: Report of a Consensus Workshop of the Cancer Immunotherapy Consortium of the Cancer Research Institute. *Cancer Immunol. Res.* **4**, 279–288 (2016).
2. Ocana, A., Pandiella, A., Siu, L. L. & Tannock, I. F. Preclinical development of molecular-targeted agents for cancer. *Nat. Rev. Clin. Oncol.* **8**, 200–209 (2010).
3. Cassidy, J. W., Caldas, C. & Bruna, A. Maintaining tumor heterogeneity in patient-derived tumor xenografts. *Cancer Res.* **75**, 2963–2968 (2015).
4. Hutchinson, L. & Kirk, R. High drug attrition rates—where are we going wrong? *Nat. Rev. Clin. Oncol.* **8**, 189 (2011).
5. Shultz, L. D., Ishikawa, F. & Greiner, D. L. Humanized mice in translational biomedical research. *Nat. Rev. Immunol.* **7**, 118–130 (2007).
6. Horowitz, L. F. *et al.* Multiplexed drug testing of tumor slices using a microfluidic platform. *Nat. Precis. Oncol.* **4**, 12 (2020).
7. Ayuso, J. M., Park, K. Y., Virumbrales-Muñoz, M. & Beebe, D. J. Toward improved in vitro models of human cancer. *APL Bioeng.* **5**, (2021).
8. Bejarano, L., Jordão, M. J. & Joyce, J. A. Therapeutic Targeting of the Tumor Microenvironment. *Cancer Discov.* **11**, 933–959 (2021).
9. Zhang, J. *et al.* Immunotherapy discovery on tumor organoid-on-a-chip platforms that recapitulate the tumor microenvironment. *Adv. Drug Deliv. Rev.* **187**, 114365 (2022).
10. Mehta, G., Hsiao, A. Y., Ingram, M., Luker, G. D. & Takayama, S. Opportunities and challenges for use of tumor spheroids as models to test drug delivery and efficacy. *J. Control. Release* **164**, 192–204 (2012).
11. Dorrigiv, D. *et al.* Microdissected tissue vs tissue slices—a comparative study of tumor explant models cultured on-chip and off-chip. *Cancers (Basel).* **13**, 4208 (2021).
12. Moore, N. *et al.* A multiplexed microfluidic system for evaluation of dynamics of immune-tumor interactions. *Lab Chip* **18**, 1844–1858 (2018).
13. Eduati, F. *et al.* A microfluidics platform for combinatorial drug screening on cancer biopsies. *Nat. Commun.* **9**, 2434 (2018).
14. Akhtar, A. The Flaws and Human Harms of Animal Experimentation. *Cambridge Q. Healthc. Ethics* **24**, 407–419 (2015).
15. Jin, M. Z. *et al.* Organoids: An intermediate modeling platform in precision oncology. *Cancer Lett.* **414**, 174–180 (2018).
16. Ghaemmaghami, A. M., Hancock, M. J., Harrington, H., Kaji, H. & Khademhosseini, A. Biomimetic tissues on a chip for drug discovery. *Drug Discov. Today* **17**, 173–181 (2012).
17. Sontheimer-Phelps, A., Hassell, B. A. & Ingber, D. E. Modelling cancer in microfluidic human organs-on-chips. *Nat. Rev. Cancer* **19**, 65–81 (2019).
18. van de Wetering, M. *et al.* Prospective Derivation of a Living Organoid Biobank of Colorectal Cancer Patients. *Cell* **161**, 933–945 (2015).
19. Sachs, N. *et al.* A Living Biobank of Breast Cancer Organoids Captures Disease Heterogeneity. *Cell* **172**, 373-386.e10 (2018).
20. Kopper, O. *et al.* An organoid platform for ovarian cancer captures intra- and interpatient heterogeneity. *Nat. Med.* **25**, 838–849 (2019).
21. Gray, H. J. *et al.* Extraordinary clinical response to ibrutinib in low-grade ovarian cancer guided by organoid drug testing. *npj Precis. Oncol.* **7**, 45 (2023).
22. Li, X. *et al.* Navigating metabolic pathways to enhance antitumour immunity and immunotherapy. *Nat. Rev. Clin. Oncol.* **16**, 425–441 (2019).

23. Dougan, M., Dranoff, G. & Dougan, S. K. Cancer Immunotherapy: Beyond Checkpoint Blockade. *Annu. Rev. Cancer Biol.* **3**, 55–75 (2019).
24. Kruger, S. *et al.* Advances in cancer immunotherapy 2019 – latest trends. *J. Exp. Clin. Cancer Res.* **38**, 268 (2019).
25. Letai, A. Functional precision cancer medicine—moving beyond pure genomics. *Nat. Med.* **23**, 1028–1035 (2017).
26. Murciano-Goroff, Y. R., Warner, A. B. & Wolchok, J. D. The future of cancer immunotherapy: microenvironment-targeting combinations. *Cell Res.* **30**, 507–519 (2020).
27. Xin Yu, J. *et al.* Trends in clinical development for PD-1/PD-L1 inhibitors. *Nat. Rev. Drug Discov.* **19**, 163–164 (2020).
28. Jonas, O. *et al.* An implantable microdevice to perform high-throughput in vivo drug sensitivity testing in tumors. *Sci. Transl. Med.* **7**, 284ra57 (2015).
29. Klinghoffer, R. A. *et al.* A technology platform to assess multiple cancer agents simultaneously within a patient's tumor. *Sci. Transl. Med.* **7**, 284ra58-284ra58 (2015).
30. Tatarova, Z. *et al.* A multiplex implantable microdevice assay identifies synergistic combinations of cancer immunotherapies and conventional drugs. *Nat. Biotechnol.* **40**, 1823–1833 (2022).
31. Sivakumar, R. *et al.* Organotypic tumor slice cultures provide a versatile platform for immuno-oncology and drug discovery. *Oncoimmunology* **8**, e1670019 (2019).
32. Vaira, V. *et al.* Preclinical model of organotypic culture for pharmacodynamic profiling of human tumors. *Proc. Natl. Acad. Sci.* **107**, 8352–8356 (2010).
33. Majumder, B. *et al.* Predicting clinical response to anticancer drugs using an ex vivo platform that captures tumour heterogeneity. *Nat. Commun.* **6**, 6169 (2015).
34. Jagatia, R. *et al.* Patient-derived precision cut tissue slices from primary liver cancer as a potential platform for preclinical drug testing. *eBioMedicine* **97**, 104826 (2023).
35. Franko, A. J. & Koch, C. J. Binding of misonidazole to V79 spheroids and fragments of dunning rat prostatic and human colon carcinomas in vitro: Diffusion of oxygen and reactive metabolites. *Int. J. Radiat. Oncol. Biol. Phys.* **10**, 1333–1336 (1984).
36. Evans, S. M., Jenkins, W. T., Joiner, B., Lord, E. M. & Koch, C. J. 2-Nitroimidazole (EF5) binding predicts radiation resistance in individual 9L s.c. tumors. *Cancer Res.* **56**, 405–411 (1996).
37. Ricciardelli, C. *et al.* Novel ex vivo ovarian cancer tissue explant assay for prediction of chemosensitivity and response to novel therapeutics. *Cancer Lett.* **421**, 51–58 (2018).
38. Polak, R., Zhang, E. T. & Kuo, C. J. Cancer organoids 2.0: modelling the complexity of the tumour immune microenvironment. *Nat. Rev. Cancer* **24**, 523–539 (2024).
39. Wu, K. Z. *et al.* Making In Vitro Tumor Models Whole Again. *Adv. Healthc. Mater.* **12**, 2202279 (2023).
40. Powley, I. R. *et al.* Patient-derived explants (PDEs) as a powerful preclinical platform for anti-cancer drug and biomarker discovery. *Br. J. Cancer* **122**, 735–744 (2020).
41. Demetriou, C. *et al.* An optimised patient-derived explant platform for breast cancer reflects clinical responses to chemotherapy and antibody-directed therapy. *Sci. Rep.* **14**, 12833 (2024).
42. Aref, A. R. *et al.* Screening therapeutic EMT blocking agents in a three-dimensional microenvironment. *Integr. Biol.* **5**, 381–389 (2013).
43. Aref, A. R. *et al.* 3D microfluidic ex vivo culture of organotypic tumor spheroids to model immune checkpoint blockade. *Lab Chip* **18**, 3129–3143 (2018).
44. Jenkins, R. W. *et al.* Ex vivo profiling of PD-1 blockade using organotypic tumor spheroids. *Cancer Discov.* **8**, 196–215 (2018).
45. Li, X. *et al.* Oncogenic transformation of diverse gastrointestinal tissues in primary organoid culture. *Nat. Med.* **20**, 769–777 (2014).
46. Neal, J. T. *et al.* Organoid Modeling of the Tumor Immune Microenvironment. *Cell* **175**, 1972-

1988.e16 (2018).
47. Astolfi, M. *et al.* Micro-dissected tumor tissues on chip: an ex vivo method for drug testing and personalized therapy. *Lab Chip* **16**, 312–325 (2016).
48. Chatzidimitriou, F. A Platform to Restore Intra-Tissue Flow in Live Explant Assays. *Ph.D. thesis, Imperial College London (Bioengineering Department)* (2021). doi:https://doi.org/10.25560/100935
49. Crosby, D. *et al.* Early detection of cancer. *Science* **375**, 1244 (2022).
50. Horowitz, L. F. *et al.* Microdissected "cuboids" for microfluidic drug testing of intact tissues. *Lab Chip* **21**, 122 (2021).
51. Lockhart, E. J. *et al.* Drug testing of monodisperse arrays of live microdissected tumors using a valved multiwell microfluidic platform. *Lab Chip* **24**, 2683 (2024).
52. Stepanov, I. *et al.* Low-Cost Robotic Manipulation of Live Microtissues for Cancer Drug Testing. *BioRxiv* https://doi.org/10.1101/2024.03.21.586169 (2024).
53. Groebe, K. & Mueller-Klieser, W. On the relation between size of necrosis and diameter of tumor spheroids. *Int. J. Radiat. Oncol.* **34**, 395–401 (1996).
54. Singh, M. *et al.* Controlled Three-Dimensional Tumor Microenvironments Recapitulate Phenotypic Features and Differential Drug Response in Early vs Advanced Stage Breast Cancer. *ACS Biomater. Sci. Eng.* **4**, 421–431 (2018).
55. Aguilera, T. A. *et al.* Reprogramming the immunological microenvironment through radiation and targeting Axl. *Nat. Commun.* **7**, 13898 (2016).
56. Sathe, A. *et al.* Colorectal Cancer Metastases in the Liver Establish Immunosuppressive Spatial Networking between Tumor-Associated SPP1+ Macrophages and Fibroblasts. *Clin. Cancer Res.* **29**, 244–260 (2023).
57. Bazzichetto, C. *et al.* Interleukin-8 in Colorectal Cancer: A Systematic Review and Meta-Analysis of Its Potential Role as a Prognostic Biomarker. *Biomedicines* **10**, 2631 (2022).
58. Itatani, Y. *et al.* The Role of Chemokines in Promoting Colorectal Cancer Invasion/Metastasis. *Int. J. Mol. Sci.* **17**, 643 (2016).
59. Morris, V. K. *et al.* Treatment of Metastatic Colorectal Cancer: ASCO Guideline. *J. Clin. Oncol.* **41**, 678–700 (2023).
60. Switzer, B., Puzanov, I., Skitzki, J. J., Hamad, L. & Ernstoff, M. S. Managing Metastatic Melanoma in 2022: A Clinical Review. *JCO Oncol. Pract.* **18**, 335–351 (2022).
61. Rodriguez, H., Zenklusen, J. C., Staudt, L. M., Doroshow, J. H. & Lowy, D. R. The next horizon in precision oncology: Proteogenomics to inform cancer diagnosis and treatment. *Cell* **184**, 1661–1670 (2021).
62. Rosenberger, F. A. *et al.* Spatial single-cell mass spectrometry defines zonation of the hepatocyte proteome. *Nat. Methods* **20**, 1530–1536 (2023).
63. Martínez-Val, A. *et al.* Hybrid-DIA: intelligent data acquisition integrates targeted and discovery proteomics to analyze phospho-signaling in single spheroids. *Nat. Commun.* **14**, 3599 (2023).
64. Myers, S. A. *et al.* Streamlined protocol for deep proteomic profiling of FAC-sorted cells and its application to freshly isolated murine immune cells. *Mol. Cell. Proteomics* **18**, 995–1009 (2019).
65. Satpathy, S. *et al.* Microscaled proteogenomic methods for precision oncology. *Nat. Commun.* **11**, 532 (2020).
66. Armstrong, H. K. *et al.* Dysregulated fibronectin trafficking by Hsp90 inhibition restricts prostate cancer cell invasion. *Sci. Rep.* **8**, 2090 (2018).
67. van Maldegem, F. *et al.* Characterisation of tumour microenvironment remodelling following oncogene inhibition in preclinical studies with imaging mass cytometry. *Nat. Commun.* **12**, 5906 (2021).
68. Gujral, T. S. *et al.* Profiling phospho-signaling networks in breast cancer using reverse-phase

protein arrays. *Oncogene* **32**, 3470–3476 (2013).
69. Hubert, C. G. *et al.* A three-dimensional organoid culture system derived from human glioblastomas recapitulates the hypoxic gradients and cancer stem cell heterogeneity of tumors found in vivo. *Cancer Res.* **76**, 2465–2477 (2016).
70. Li, J. *et al.* TMTpro reagents: a set of isobaric labeling mass tags enables simultaneous proteome-wide measurements across 16 samples. *Nat. Methods* **17**, 399 (2020).
71. Edwards, N. J. *et al.* The CPTAC data portal: A resource for cancer proteomics research. *J. Proteome Res.* **14**, 2707–2713 (2015).
72. Whiteaker, J. R. *et al.* CPTAC Assay Portal: a repository of targeted proteomic assays. *Nat. Methods* **11**, 703–704 (2014).
73. van Bentum, M. & Selbach, M. An Introduction to Advanced Targeted Acquisition Methods. *Mol. Cell. Proteomics* **20**, 100165 (2021).
74. Stopfer, L. E. *et al.* High-Density, Targeted Monitoring of Tyrosine Phosphorylation Reveals Activated Signaling Networks in Human Tumors. *Cancer Res.* **81**, 2495 (2021).
75. Summers, H. D., Wills, J. W. & Rees, P. Spatial statistics is a comprehensive tool for quantifying cell neighbor relationships and biological processes via tissue image analysis. *Cell Reports Methods* **2**, 100348 (2022).
76. Carr, S. A. *et al.* Targeted peptide measurements in biology and medicine: Best practices for mass spectrometry-based assay development using a fit-for-purpose approach. *Mol. Cell. Proteomics* **13**, 907–917 (2014).
77. Ryu, H. *et al.* Transparent, Compliant 3D Mesostructures for Precise Evaluation of Mechanical Characteristics of Organoids. *Adv. Mater.* **33**, 2100026 (2021).
78. Nguyen, T. N. H. *et al.* Label-Free, Real-Time Monitoring of Cytochrome C Drug Responses in Microdissected Tumor Biopsies with a Multi-Well Aptasensor Platform. *Sci. Adv.* in press (2024).
79. Li, W., Germain, R. N. & Gerner, M. Y. High-dimensional cell-level analysis of tissues with Ce3D multiplex volume imaging. *Nat. Protoc.* **14**, 1708–1733 (2019).
80. Schindelin, J. *et al.* Fiji: An open-source platform for biological-image analysis. *Nat. Methods* **9**, 676–682 (2012).

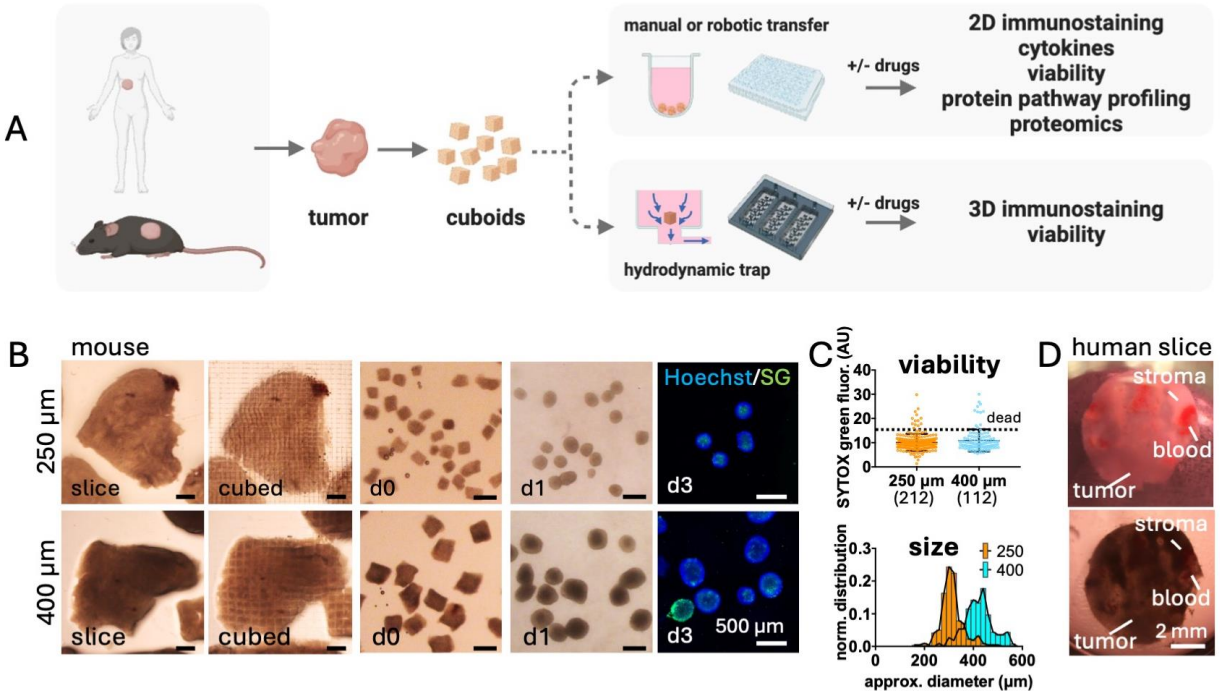

Figure 1: Cuboid generation and culture. (**A**) Schematic of cuboid workflow. (**B**) Sequential formation and culture of 250- µm or 400-µm mouse Py8119 breast cancer syngeneic tumor cuboids, with vibratome sectioning to make slices, tissue chopper to make polygonal cuboids (day 0), and spherical morphology at day 1 and day 3. Viability was assessed at day 3 using the SYTOX green dye (SG) for dead nuclei and the Hoechst blue dye for all nuclei. Cuboids were cultured in 6-well plates. (**C**) Graphs of viability (ave. ± S.D.; dashed line for viability cutoff) and size (histogram) of cuboids at day 3. (**D**) Patient colorectal cancer liver metastasis (CRClm) slice visualized with either top illumination or through illumination (bottom).

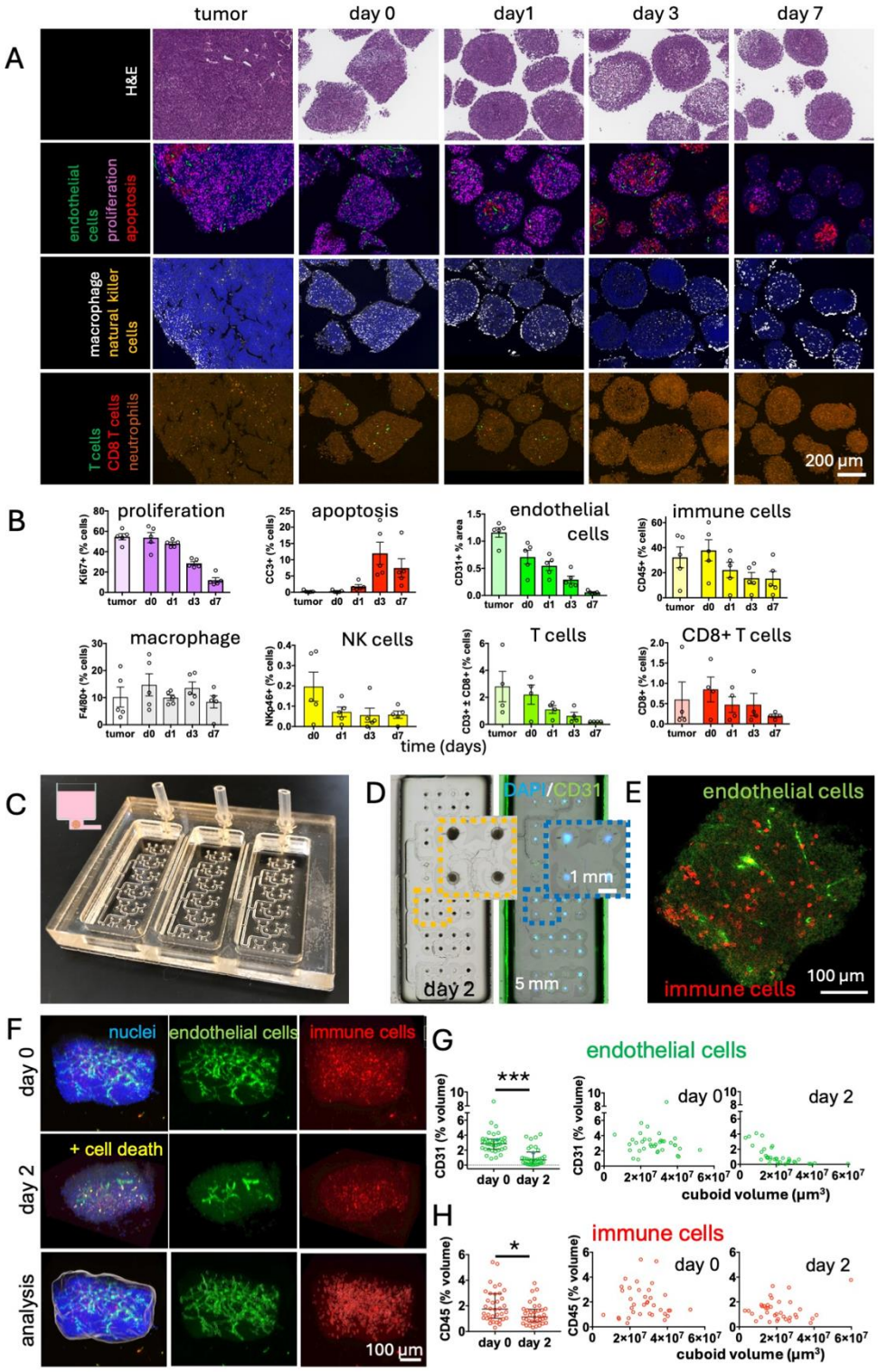

Figure 2: Characterization of the mouse cuboid and its TME. (**A,B**) Histology and fluorescent multi-immunohistochemistry (multi-IHC) of mouse Py8119 breast cancer cuboids. (**A**) Histology (H&E) and multi-IHC for apoptotic cell death (cleaved-caspase 3, CC3), proliferation (Ki67) multiple cell types. (**B**) Quantitation of cell staining in (**A**). Ave. ± sem. N=5 tumors each day. Individual points represent the mean

value for that time point for the total surface area encompassing multiple cuboids (11-40) for each tumor. (**C-H**) Whole-mount immunostaining of Py8119 mouse cuboids at day 0 and day 2. (**C**) Microfluidic device used for on-device immunostaining, clearing, and confocal imaging. 3 independent wells each have 48 cuboid traps each connected by binaries to 1 output. (**D**) One well showing Py8119 mouse cuboids in the device after 2 days in culture and immunostaining (CD31 for endothelial cells, CD45 for immune cells, cleaved-caspase-3 for cell death, DAPI nuclear stain), and clearing with Ce3D. (**E**) Confocal image of immunostaining for day 0. (**F**) 3D images of staining with example of Imaris 3D analysis for day 0. (**G,H**) Graphs showing quantitation of endothelial and immune cell staining for individual cuboids (points). Median and quartile bars in black. n=34-36 cuboids. Mann-Whitney test. *$p<0.05$, ***$p<0.0001$. Endothelial cells (CD31), immune cells (CD45), macrophage (F4/80), NK cells (NKp46), T cells (CD3), cytotoxic T cells (CD8), and neutrophils (Ly6G).

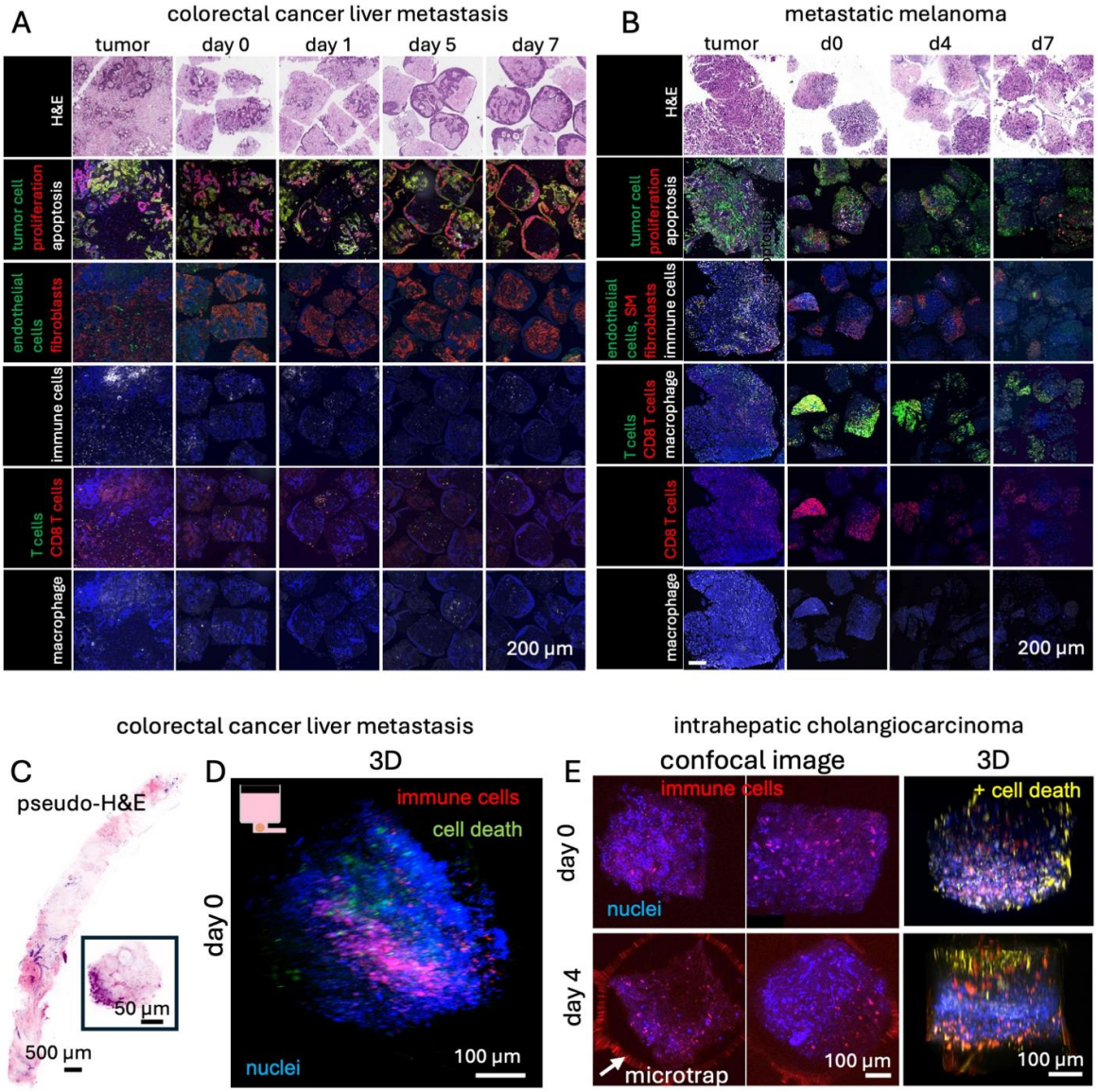

Figure 3. Characterization of heterogeneous patient cancer cuboids and their TME. (**A,B**) Histology and multi-IHC of a colorectal cancer liver metastasis (CRClm) (**A**) and a patient metastatic melanoma lymph node (**B**). Cuboids were cultured in 6-well plates. Cell type antibodies: tumor cells (colon cancer: AE1/AE2; melanoma: Mel mix), endothelial cells (CD31), fibroblasts and smooth muscle cells (smooth muscle actin), immune cells (CD45), macrophage (human: CD68), T cells (CD3), and cytotoxic T cells (CD8). (**C**) Pseudo-H&E optical section of a needle biopsy and cuboid (inset) from a CRClm. (**D**) 3D Imaris image from confocal images of a cuboid from a CRClm after 3D immunostaining with CD45 for immune cells, cleaved-caspase-3 for cell death, and a DAPI nuclear stain. (**E**) 2D confocal images and 3D Imaris images of cuboids from a patient idiopathic cholangiocarcinoma (ICC) at day 0 or after 4 days culture in the microfluidic device.

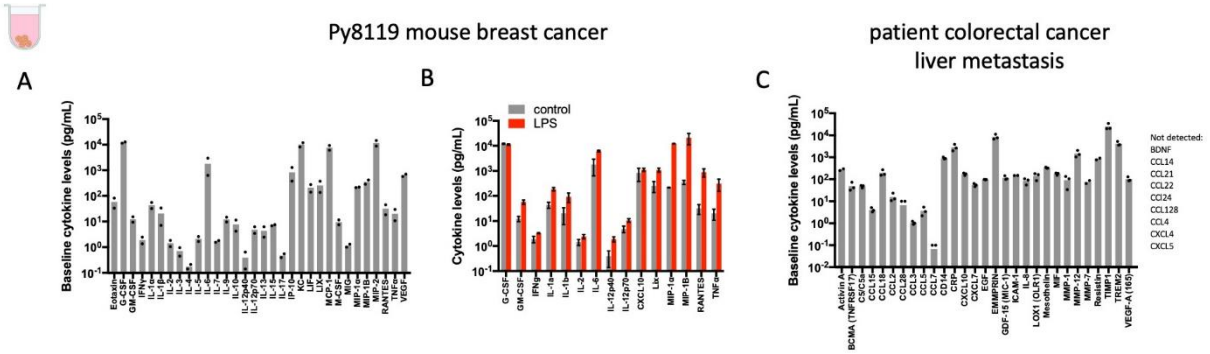

Figure 4. Immune cell-dependent responses in cuboids in a 96-well plate. Cytokine/chemokine secretion in cuboids grown in 96 well plates, measured by Luminex. (**A,B**) Cytokine secretion from Py8119 mouse breast cancer cuboids, with baseline secretion of a panel of 31 cytokines (**A**) and for a subset, after exposure to LPS (lipopolysaccharide, 1 µg/mL for 24 hours) to activate the innate immune system versus control (**B**). 2-6 cuboids/well. Individual replicates shown. (**C**) Baseline cytokine secretion from human colorectal cancer liver metastasis cuboids (4-6 cuboids per well, day 5).

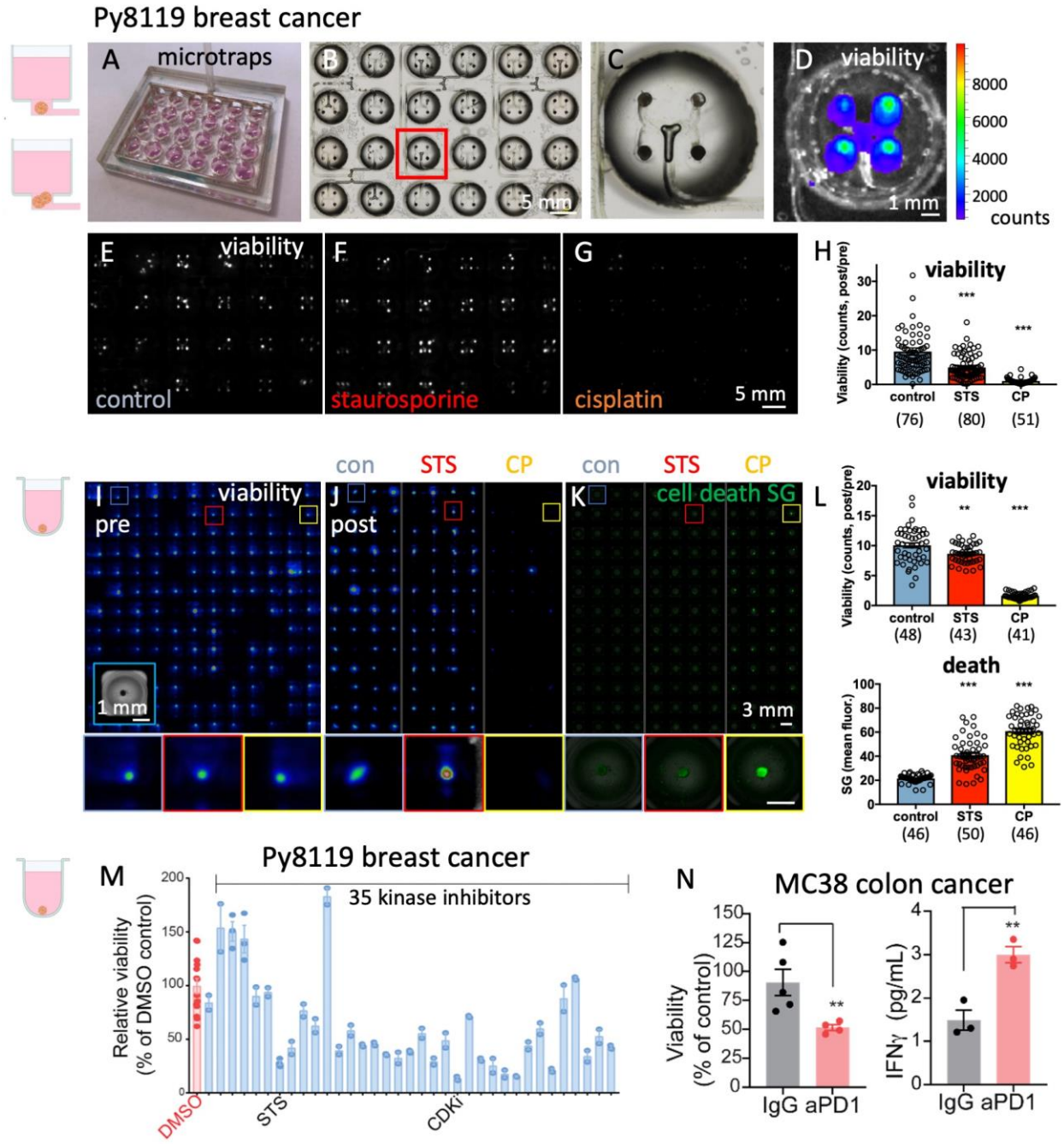

Figure 5. Drug treatment of mouse tumor cuboids. Py8119 mouse breast cancer cuboids were treated in parallel either on a microfluidic device (**A-H**) or with individual cuboids in a 384-well plate (I-M). (**A**) Microfluidic device with 24 wells, 4 traps/well. (**B-D**) Py8119 mouse breast cancer cuboids loaded on a device (**B, C** close-up) with viability by RealTime-Glo (RTG) luminescence imaging (**D**). (**E-G**) Viability after 3 days of drug treatment of 3 different devices with staurosporine (STS, 2 µM) or cisplatin (CP, 100 µM). (**H**) Graph shows changes in viability (post/pre) by luminescence for individual traps (1-3 cuboids each trap). Ave. ± sem. Kruskal-Wallis test versus control with Dunns multiple comparisons. ***p<0.001. (I-K)

Drug responses of individual cuboids, manually pipetted to have one per well on a 384-well plate, measured for viability by RealTime-Glo (RTG) luminescence (**I,J**) and for cell death by SYTOX green (SG) nuclear stain (**K**). Close-ups shown below. (**L**) Graphs of viability and cell death, with responses of individual cuboids (circles) and ave. ± sem. One way ANOVA, Tukey post-hoc. ***$p<0.0005$. N=41-50. (**M**) Responses of mouse Py8119 cuboids to a panel of 34 kinase inhibitors (1 µM). Viability (post/pre) measured by RTG luminescence before and after 3 day treatment, given as a % of the DMSO control. Duplicates of 2-6 cuboids/well. Staurosporine (STS) and CDK4/6 (CDKi) kinase inhibitor positive controls. (**N**) Responses of MC38 subcutaneous mouse colon cancer cuboids to checkpoint inhibitor immunotherapy for 4 days with anti-PD-1 versus IgG control, with decreased viability (RTG) and increased IFNγ secretion. 6-12 cuboids per well. Ave. ± sem. Student's T-test **$p<0.01$.

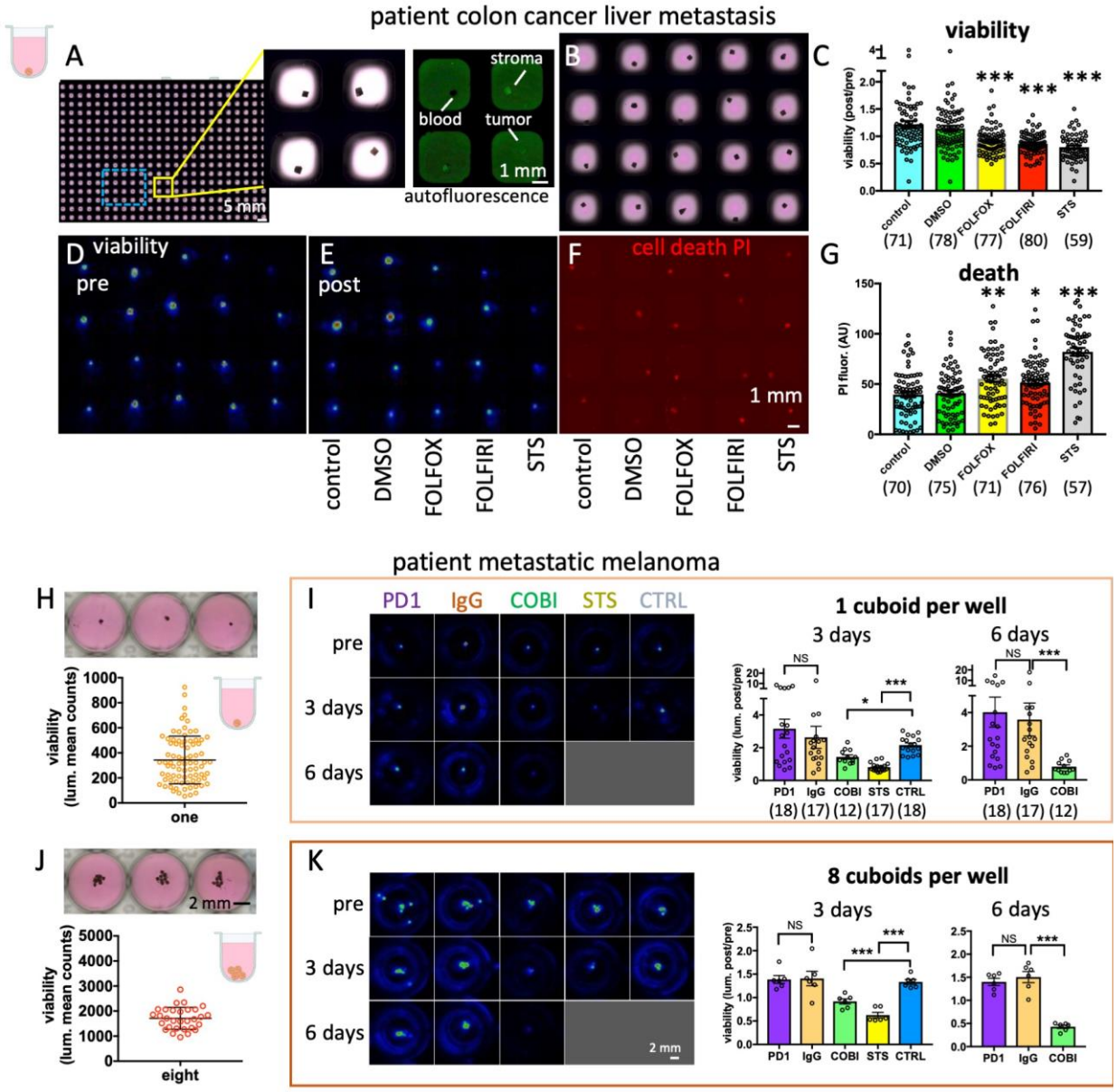

Figure 6. Drug treatment of human cuboids. (**A-G**) Drug treatment of patient colorectal cancer liver metastasis cuboids, transferred by a robot to a 384-well plate (**A**), with 1 cuboid per well and close-ups of yellow region showing heterogeneity revealed by green autofluorescence. After exposure to drugs for 5 days, viability was measured by Realtime-Glo (RTG) luminescence and death was measured by propidium iodide (PI). (**B, D-F**) Close-ups of blue rectangle in (**A**), with pre-treatment RTG viability on day 2 (**D**), and day 7 post treatment RTG viability (**E**) and propidium iodide staining for cell death. (**F**) Graph of viability by RTG with post/pre for each cuboid. (**G**) Graph of cell death by PI. Responses of individual cuboids (circles) and average ± sem. Kruskal-Wallis test with Dunn's multiple comparison. 8 wells with two cuboids per well not included. DMSO (0.2%). FOLFOX (1 µg/mL 5-fluorouracil, 1 µg/mL oxaliplatin). FOLFIRI (1 µg/mL 5-fluorouracil, 2 µg/mL irinotecan), STS (staurosporine 1 µM). Ave. ± sem. Kruskal-Wallis test with Dunn's multiple comparisons versus DMSO. *p<0.05. **p<0.01. ***p<0.0005. (**H-K**) Cuboids from positive lymph nodes from a patient metastatic melanoma treated for 6 days with

checkpoint inhibitor (PD-1), IgG control, the MEK kinase inhibitor cobimetinib (COBI, 1 µM), staurosporine (STS), or control (CTRL). (**H,J**) Cuboids image and graph of RTG viability for individual cuboids at day 1 for single (**H**) or for eight (**J**) cuboids per well. (**I,J**) Representative images of RTG viability and graphs (post/pre) for one (**I**) or for two (**J**) cuboids per well. Number of wells indicated for single cuboid wells, n=6 for eight cuboid wells. Mann-Whitney and Kruskal-Wallis rank order tests. *$p<0.05$. ***$p<0.001$.

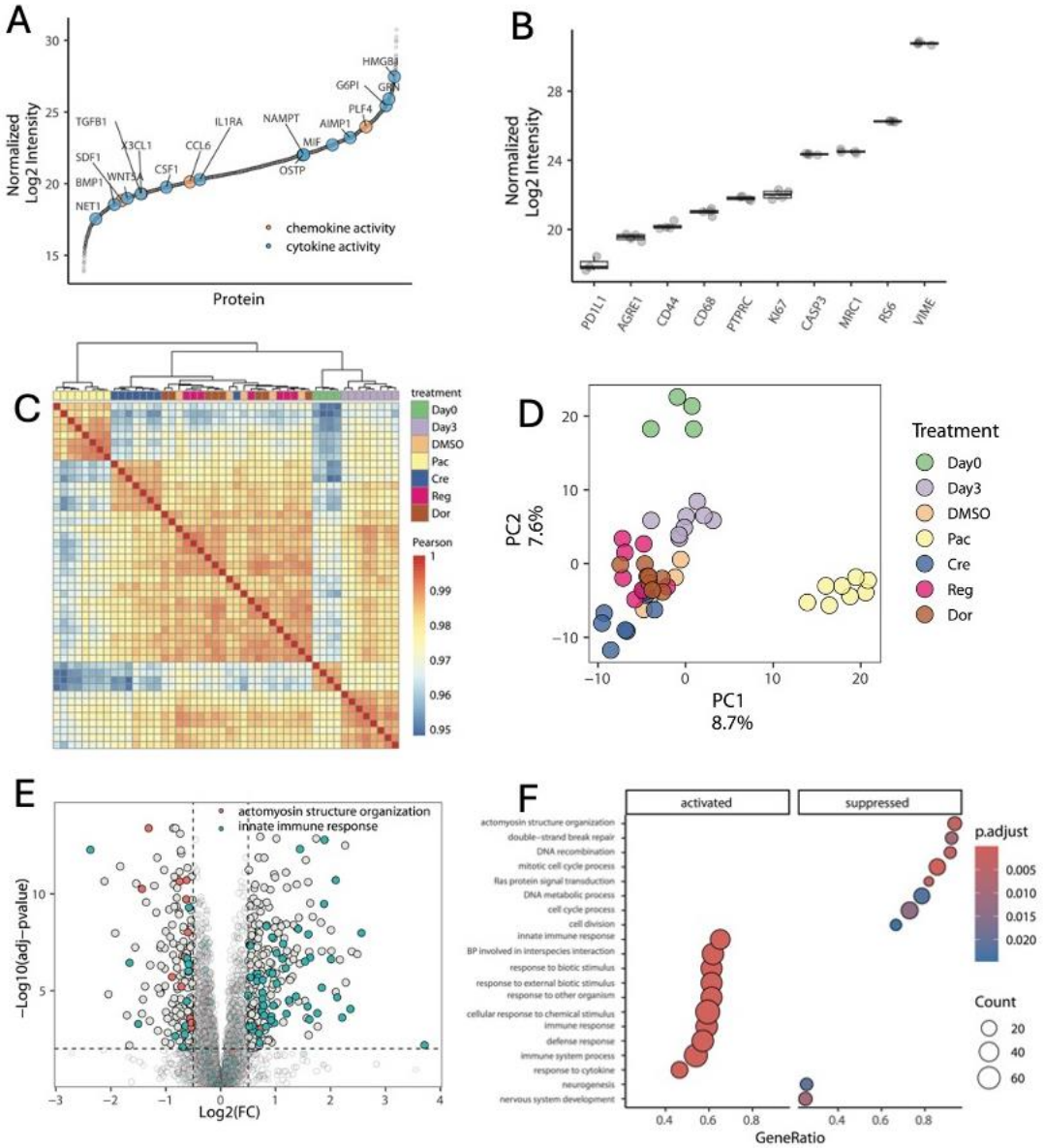

Figure 7. Profiling PY8119 breast cuboid proteomes using mass spectrometry and its changes upon drug treatments. Quantification of TME proteins: (**A**) Ranked plot for median normalized log2 protein intensities in Day1 samples; highlighted proteins associated with GO terms: chemokine (yellow) and cytokine activities (blue). (**B**) Box and Dot plot of Day 1 normalized protein log2 intensities for observed TME markers.[67] Observed changes to the cuboid proteome upon drug treatment. (**C**) Heat map: Pearson correlations for protein abundances across drug treatments and replicates. (Day1, Day3: 0.5 untreated-day 3, **DMSO**: 0.1% DMSO-day 3, **Pac**: 10 µM paclitaxel-day 3, **Cre**: 0.5 µM crenolanib-day 3, **Reg**: 0.5 µM regorafenib-day 3, **Dor**: 0.5 µM doramapimod-day3). (**D**) Dot plot: PC1 and PC2 of principal component analysis for protein abundance measurements across treatments and replicates. (**E**) Volcano plot: protein abundance log2 fold changes between DMSO and Paclitaxel treatments on day 3 and adjusted p-values. Log2 fold changes and multiple hypothesis testing adjusted p-values were calculated using MSStats linear model. Highlighted proteins in (**grey**) with fold change threshold

|Log2FC| > 0.5 and adjusted p-value<0.01; associated with Gene Ontology terms: (**blue**) innate immune response, (**red**) actomyosin structure organization. (**F**) Gene Ontology enrichment analysis of Biological Process terms for upregulated and downregulated proteins between DMSO and Paclitaxel treatments

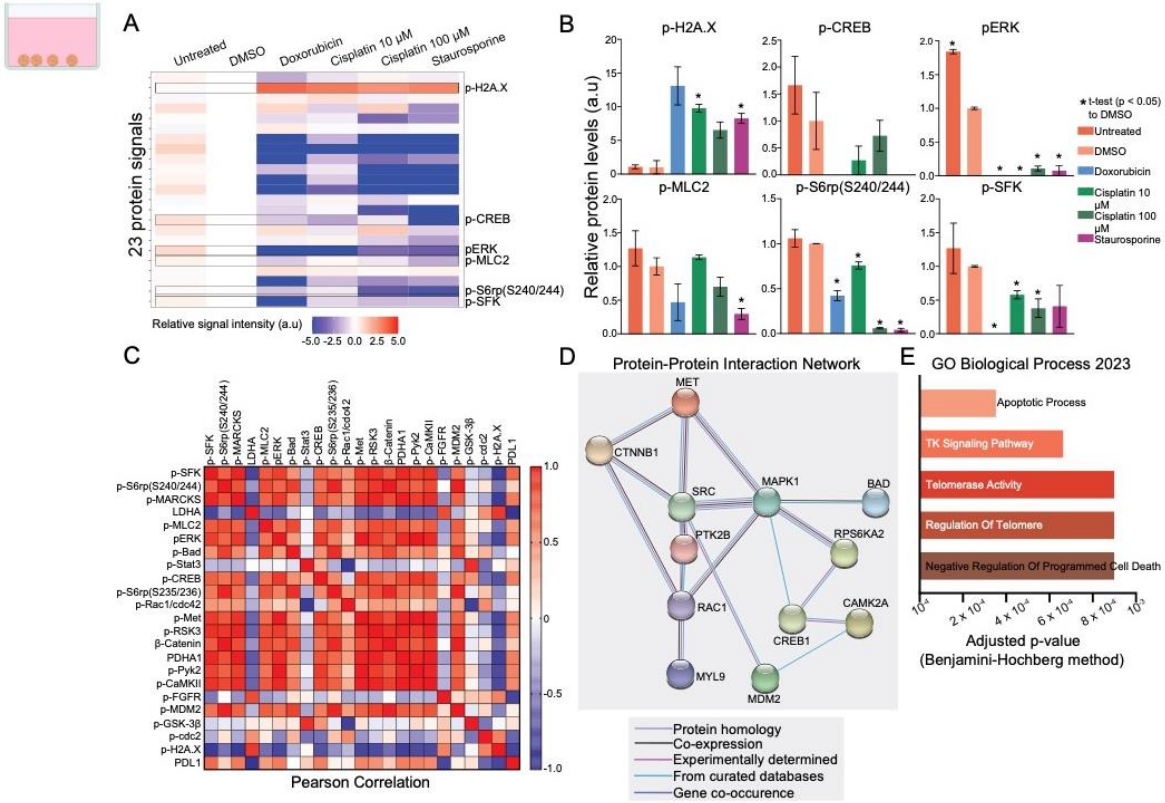

Figure 8. Profiling changes in signaling pathways from drug treated PY8119 breast cuboids. Reverse-phase protein array (RPPA) was used to profile 48 proteins from PY8119 breast cuboid samples after treatment for 3 days (untreated, 0.1% DMSO, Doxorubicin 10 µM, Cisplatin 10 µM, Cisplatin 100 µM, or Staurosporine 2 µM). Data from the 23 high-quality signals are shown. (**A**) Heat map representation of relative signal intensities, normalized in a stepwise manner: beta-actin levels, untreated samples, and DMSO treated samples. (**B**) Graphical representation of relative protein levels from annotated proteins in (A), normalized in the same process as in (**A**) except without log2 transformation. n=2 per condition. *$p < 0.05$ unpaired t-tests compared to DMSO. (**C**) Pearson Correlation. The correlation matrix depicts the result of a Pearson correlation analysis performed on the 23 proteins of interest using measurements taken from all samples. (**D**) Protein-protein interaction network from positively correlated proteins in (**C**) (StringDB). (**E**) Gene enrichment analysis using the same positively correlated proteins from (**C**) (Enrichr). Adjusted p-values corrected for multiple hypothesis testing by the Benjamini-Hochberg method. Full names of top biological processes: regulation of apoptotic process, transmembrane receptor protein tyrosine kinase signaling pathway, regulation of telomerase activity, and regulation of telomere maintenance via telomerase.